Engineering III-N Alloys and Devices for Photovoltaic Progress

by

Joshua J. Williams

A Dissertation Presented in Partial Fulfillment
of the Requirements for the Degree
Doctor of Philosophy

Approved June 2016 by the
Graduate Supervisory Committee:

Christiana Honsberg, Co-Chair
Stephen Goodnick, Co- Chair
Richard King
Todd Williamson
Terry Alford

ARIZONA STATE UNIVERSITY

August 2016

ABSTRACT

The state of the solar industry has reached a point where significant advancements in efficiency will require new materials and device concepts. The material class broadly known as the III-N's have a rich history as a commercially successful semiconductor. Since discovery in 2003 these materials have shown promise for the field of photovoltaic solar technologies. However, inherent material issues in crystal growth and the subsequent effects on device performance have hindered their development. This thesis explores new growth techniques for III-N materials in tandem with new device concepts that will either work around the previous hindrances or open pathways to device technologies with higher theoretical limits than much of current photovoltaics. These include a novel crystal growth reactor, efforts in production of better quality material at faster rates, and development of advanced photovoltaic devices: an inversion junction solar cell, material work for hot carrier solar cell, ground work for a selective carrier contact, and finally a refractory solar cell for operation at several hundred degrees Celsius.

DEDICATION

I would like to thank my family members for all their love and support. To my mother and father, who raised me to be open-minded and encouraged me to explore my dreams even if they took me across the country. To my siblings, who one after another demonstrated the paths to success and were there to support and advise me on my own.

I would like to acknowledge all the great friends I have made here in Arizona both in the academic community and the outdoors community. You have helped to keep my spirits up even when the graduate school process was at its hardest.

I wish to thank my best friends, Brian Fane and Andrew Schmalzer, who have always been, and will always be there. Andrew, you beat us to it. Brian, you'll finish soon. No matter what happens in life, I'll see you both in the mountains.

Thank you, Casey, for standing by my side for the past three years.

Let this thesis mark the end of one chapter and the beginning of another.

ACKNOWLEDGMENTS

First and foremost, I want to acknowledge my committee members. To my co-advisors Dr. Christiana Honsberg and Dr. Stephen Goodnick. Dr. Honsberg, thank you for giving me the opportunity to research solar and InGaN simultaneously. Thank you for supporting me, giving me guidance, and telling it like it is. Dr. Goodnick, thank you for being a shining example of professionalism in a chaotic academic community.

I would like to thank Dr. Terry Alford for serving on my committee, for going out of his way to make interdepartmental Ph.D. research possible, and for helping me stay focused on the ultimate task with so many day-to-day distractions. I would like to thank Dr. Richard King for giving guidance in the field of photovoltaics and helping to shape the final year of my doctoral work.

Last but not least I want to thank Dr. Todd Williamson. Todd, thank you for teaching me about growth technologies, about laboratory practices, and about politics even in a scientific work place. Thank you, for standing beside me and supporting me when what was right was not what was easy. You taught me much both in and out of the lab. It would be a great honor to someday be as good a mentor to someone else.

Thanks be to all of my colleagues at Arizona State University. My friends in the Nano & III-V Group: Matthias, Aymeric, Ehsan, Chaomin, and Dr. Faleev. Thanks to all the others at the Solar Power Laboratory including Dr. Stuart Bowden and Bill Dauksher. Thanks to my closest collaborators on the FOCUS project Dr. Heather McFavilen, Dr. Ding Ding, and Dr. Alec Fischer. Thanks to the staff at the LeRoy Eyring Center for keeping such a facility running and for being helpful about getting things back up when they weren't.

Finally, I'd like to acknowledge my funding agencies, without whom none of this would have been possible.

TABLE OF CONTENTS

LIST OF TABLES

LIST OF FIGURES

LIST OF ABBREVIATIONS

AlN – aluminum-nitride

AFM – atomic force microscopy

a_x – lattice parameter

CSC – carrier-selective contact

CPV – concentrator photovoltaics

CSP – concentrated solar power

DC – double crystal

ENABLE – energetic neutral atom beam lithography and epitaxy

ε – lattice strain

EQE – external quantum effeciency

ESC – energy-selective contact

FWHM – full-width at half-maximum

FF – fill-factor

GaN – gallium-nitride

HIPSS – high-intensity pulsed solar simulator

IQE – internal quantum effeciency

ITO – indium-tin-oxide

InGaN – indium-gallium nitride

InN – indium-nitride

I_{SC} – short circuit current

J_{SC} – short circuit current density

LCOE – levelized cost of electricity

MBE – molecular beam epitaxy

MEE – migration-enhanced epitaxy

MFC – mass-flow

MOVPE – metal organic vapor phase epitaxy

MQW – multi–quantum well

MPP – maximum power point

η – efficiency

P_{SP} – spontaneous polarization

P_{PZ} – piezoelectric polarization

PV – photovoltaic

QE – quantum efficiency

QC – quantum conversion

RHEED – reflection high–energy electron diffraction

RTD – resonant tunneling diode

RGA – residual gas analyzer

σ – sheet charge density

SQL – Shockley–Queisser limit

SCCM – standard cubic centimeter

TEM – transmission electron microscopy

TC – triple crystal

TOF – time of flight

τ – minority carrier lifetime

UID – unintentional doping

V_{OC} – open circuit voltage

W_{OC} – bandgap voltage offset

XRD – x-ray diffraction (a process) or x-ray diffractometer (a tool)

CHAPTER 1

INTRODUCTION

The most basic requirement to increase quality of life for humanity is an increase in consumption of energy per capita.[1] If humans wish an increased quality of life for all then the amount of usable energy that humanity produces must increase. Furthermore, if it should be desired that such an increase in energy production have as little environmental damage possible, then common sense would suggest that this energy be renewable.

Solar power is the most abundant renewable energy supplying planet Earth with approximately 100 million gigawatts of power.[2] Though it is inconceivable for humans to harvest all of that energy, it is also unnecessary to harvest it all. Human energy production is equal to roughly 12 thousand gigawatts, as of data circa 2012.[3] This number would be expected to double or triple as 3rd world and developing countries achieve a quality of life enjoyed by the U.S. and western European countries. Based on the aforementioned assumption of a desire for clean power, this increased power production should come from solar power.

Solar power is divided into two broad categories: solar thermal and photovoltaic (PV). Solar thermal captures the light of the sun to generate heat. This heat is used to produce steam to spin a turbine. This process is similar to fossil fuel and nuclear power plants. The concept of spinning a generator using working fluid is how all utility-scale electricity in the world is produced. Rather, that was true before the advent of photovoltaic solar power.

Photovoltaics on the other hand work on the physical phenomenon of the photoelectric effect. The photoelectric effect is a light absorption mechanism through

which a photon is absorbed by an electron in a semiconductor. Furthermore, in the photoelectric effect the energy of the photon, now belonging to the electron, excites the electron across the band gap. As more electrons are excited across the band gap from the valence band to the conduction band the material transitions from being insulating to being conductive, this is a defining feature of semiconductor materials. A photovoltaic device is one in which different types of semiconductor materials are arranged such that a built-in electric field exists to move electric charge as it is created by the photoelectric effect. The aggregate movement of electric charge is electricity. As more photovoltaic devices are wired together more electricity can be produced. This makes photovoltaic technology fundamentally different from all other power generation.

This fundamental difference in how photovoltaics produce energy mean that more than just producing renewable energy, PV can benefit society in other ways. First and foremost, photovoltaics enable the potential for distributed power. This means fewer centralized power plants and more ubiquitous electricity generation. Distributed power means better grid reliability, and lowered susceptibility to individual disasters or nefarious attacks on electric production. Additionally, the fundamental difference of photovoltaics means that power can be generated anywhere the sun shines from large-scale plants, individual businesses/homes, or even remotely as small handheld units. This enables society to have individualized electrical production.

While these benefits are undeniable, there are drawbacks to photovoltaics. Besides the obvious issue of nighttime, the primary drawbacks are based around the fact that they are limited to converting a fixed fraction of the sun's power to electrical

energy. This means that in order to collect more electricity more area needs to be covered with PV, increasing the cost. Associated with solar cells are other costs, including but not limited to structural support, electrical wiring, installation costs, and interest rates on capital investments. Therefore, with a fixed resource the only way to bring down what is known as the "levelized cost of electricity" (Cost/power produced, $/W) without reducing costs across the board is to increase the conversion efficiency.

The laws of thermodynamics dictate that the conversion efficiency of one energy form to another will always be less than 100%. In any technological field it is informative to know the theoretical limit for that conversion efficiency. The knowledge of this limit puts into perspective the feasibility of researching an incremental efficiency increase. In 1961 the team of William Shockley and Hans Queisser published a model for determining the maximum efficiency of a solar cell. Their published model, known as the Shockley-Queisser Limit (SQL), optimized the conversion efficiency based on the inputs of the solar spectrum and the semiconductor band gap. Their predicted optimum device efficiency was approximately 33% at 1.3 eV.[4] However, the assumptions made in the SQL model are not inherent to the laws of physics, but merely represent the circumstances of the majority of solar cells. By designing non-standard solar cells, the assumptions are no longer valid and devices with higher efficiencies can be realized. This leads to a new maximum conversion efficiency of 86.8%.[5], [6]

In general, the concept of engineering PV devices to operate outside the bounds of the assumptions of the SQL is an area of research that can be thought of as "advanced enablers." In order to design advanced enablers one must target an

assumption of the SQL to be contravened. For example, the record efficiency for solar cells belongs to a class of mature advanced enablers known as multijunctions. These devices overcome the assumption that a PV device has a single band gap. In these devices the solar spectrum is converted at different voltages resulting in decreased energy loss from carrier thermalization. These devices produce less current but significantly higher voltage with the end result being increased overall power.

There are other assumptions of the SQL ripe for reevaluation. The assumption that each photon will result in only one electron-hole pair can be overcome. This concept is known as multiple exciton generation and can result in low voltage devices with extraordinarily high current. Another assumption is that electrons will be extracted at the voltage defined by the band gap. Hot carrier solar cells strive to prevent thermalization, thus extracting electrons at elevated energies resulting in voltages larger than the band gap. Yet a third assumption is that sub-band gap energy photons cannot be absorbed. Intermediate band solar cells have been proposed as a method to create "stepping-stones" for absorption events such that two sub-band gap photons may be absorbed to do the work of one high-energy photon with energy greater than or equal to the band gap. These are some of the more popular ideas behind multijunctions for exceeding the SQL, but they are certainly not the only ideas.[5], [6] For all of these device concepts new research in semiconductor materials is necessary to facilitate construction of prototypes.

INDIUM-GALLIUM-NITRIDE

The material alloy system known as indium-gallium-nitride, InGaN, or $In_xGa_{1-x}N$ has a rich history in the solid-state lighting industry beginning in the 1980s. This

material system has been exclusively responsible for the advent of the blue laser, the blue LED, and the "white" LED. InGaN alloys possess several unique aspects which make them of interest as semiconductors for solar cell devices. These include but are not limited to a widely tunable band gap, strong absorptivity, spontaneous polarization, and thermal stability.

The tunable band gap of InGaN arises from the fact that is a pseudo-binary alloy of two compound semiconductors, gallium nitride and indium nitride. Gallium nitride (GaN) has a direct band gap of 3.4 eV, this allows it to absorb and emit light strongly in the near-visible ultraviolet.[7]–[10] While the band gap for gallium nitride has been relatively stable throughout research history, the indium nitride band gap has experienced a revisionary existence. Originally thought to be near 1.9 eV[9]–[11], the indium nitride band gap has been revised down to 0.9 eV[12], and even further to ~0.7 eV at cryogenic temperatures (0.65 at RT).[13]–[16] The confusion has been attributed to the presence of oxygen contamination in historic samples.[17] Though there may still be some contention to this value, most researchers agree on this value as the true band gap for InN.[18], [19] The resulting band gap for an $In_xGa_{1-x}N$ alloy (where $0 \leq x \leq 1$) follows an approximately linear interpolation between the value for indium nitride and gallium nitride. A more accurate model is a quadratic term with a bowing parameter. This bowing parameter has also been heavily revised and continues to be somewhat contentious, herein the bowing parameter will be assumed to be 1.4 eV.[20] The formula for quadratic bandgap alloying is displayed in Equation 1.1 and the values for band gap parameters in

Table *1*. Band gaps as a function of temperature are based on the Varshni equation, Equation (2).

5

$$E_G^{ABX}\{T,x\}=x \cdot E_G^{AX}\{T\}+(1-x) \cdot E_G^{BX}\{T\}-(1-x) \cdot x \cdot b^{ABX} \tag{1}$$

$$E_G\{T\}=E_G\{0\ K\}-\frac{\alpha \cdot T^2}{\beta+T} \tag{2}$$

Table 1
III-N Varshni Parameters and Bowing Parameters

	AlN	GaN	InN	$Al_xGa_{1-x}N$	$In_xAl_{1-x}N$	$In_xGa_{1-x}N$
$E_G\{0\ K\}$	6.23 eV [8]	3.51 eV [8]	0.7 eV [13]	—	—	—
A	1.799 meV/K [8]	0.909meV/K [8]	0.245 meV/K [8]	—	—	—
B	1462 K [8]	830 K [8]	624 K [8]	—	—	—
B	—	—	—	1.3 eV [21]	4.7 eV [22]	1.43 eV [20]

In direct semiconductor materials such as GaN, InN, and InGaN, the absorption of light through the photoelectric effect is the reverse process from light emission during carrier recombination of an excited electron and hole. Therefore, because gallium nitride and near gallium nitride alloys of InGaN have been used for making LEDs with strong radiative recombination, they also will absorb light very strongly. The absorptivity for GaN and InN has been measured.[23] The III-nitride material system has an absorptivity approximately an order of magnitude higher than comparable direct band gap semiconductors like GaAs and InGaP.[17], [24]–[26] As the absorptivity of a material goes up the required thickness to absorb a desired fraction of light goes down. Hence, InGaN layers require an order of magnitude less thickness than comparable semiconductors for full absorption of illumination. This is important because it helps to offset the material cost associated with indium and gallium scarcity and the resulting price of an InGaN device.

The III-nitride alloys, unlike other III-V semiconductors, have a wurtzite crystal structure. A wurtzite crystal structure is a hexagonal close packed version of

the cubic close packed zinc-blende system. This wurtzite structure arises from the non-equilateral tetrahedron formed by the molecules of group III and nitrogen. This non-equilateral tetrahedron also gives rise to an uneven charge distribution around each molecule, resulting in a local dipole. As a crystal all molecules will have the same orientation, and all dipoles are oriented parallel to the c crystal direction (001). Extrapolating the effect of the single molecule dipole to the entire crystal places a static sheet charge on either side of a semiconductor layer. This effect is known as spontaneous polarization. Spontaneous polarization can be beneficial (as in GaN-AlGaN high electron mobility transistors) or harmful (like GaN-InGaN heterojunctions in solar) in device performance, but either way it is an added complexity that must be taken into account if one is to do a thorough device design.

The aforementioned thermal stability of InGaN alloys refers to the material's chemically and electrically robust properties at elevated temperatures when compared to other semiconductors. Chemically relevant thermal stability means that the molecular bonds have higher energy than most other semiconductors. The heats of formation for GaN and InN are -117.1 and -19.3 kJ/mol, respectively.[27], [28] These lead to melting temperatures of 2792 K and 1373 K under excess nitrogen pressure, and decomposition temperatures of 1052 K and 893 K at ambient pressure, respectively.[27], [28] This enables the design of III-nitride based devices targeted for high temperature applications. The electrical stability versus temperature of InGaN alloys is assumed from the electrical stability of gallium nitride. Gallium nitride's electrical stability is based on its wide band gap and the direct effect of a wide band gap on intrinsic carrier concentration. Indium nitride with a narrower band gap will

have an intrinsic carrier population that is more temperature sensitive. Hence, the electrical stability of $In_xGa_{1-x}N$ alloys would decrease as the value of x approaches 1.

MATERIAL AND DEVICE CONSTRUCTION CHALLENGE

These properties (tunable band gap, absorptivity, polarization, and thermal stability) make indium gallium nitride of interest for building solar cells as well as many other types of semiconductor devices: light emitting diodes, lasers, high electron mobility transistors and more. However, there are challenges rooted in materials production: available substrates, heteroepitaxy, InGaN miscibility, nitrogen activation, unintentional and background doping, and magnesium incorporation and activation.

The first set of challenges are related to substrate selection, crystal lattice mismatch between different compounds, and the defects stemming from these issues. There are roughly three substrate options for growing GaN and InGaN alloys: gallium nitride, silicon, and sapphire. There are benefits and drawbacks to all of these options. The categories of for differentiating are lattice mismatch and wafer cost. Best-to-worst by lattice mismatch are GaN, sapphire, and Si with values of 0%, 13.9%, and 17% lattice mismatch to GaN respectively.[29], [30] On the other hand the costs are fairly low for both Si and sapphire wafers and orders of magnitude higher for GaN wafers. Silicon has the advantage that it enables reasonable integration of an InGaN device with other more conventional silicon based devices. However, silicon has the added drawback that the surface can be highly reactive with group III elements gallium and aluminum, forming device disrupting silicides. Sapphire, though it may be electrically

8

insulating, is chemically and thermally robust. This gives a nice stable lattice to use as a foundation for epitaxy.

The lattice mismatch in epitaxy matters because it has the strongest potential to cause device ending defects in the grown layers. These defects are formed as a free energy reduction mechanism at the molecular level. When the atoms of a new compound try to assume the lattice parameter of the existing compound at the interface, the local molecular bonds are strained. Eventually the energy built up in these strained bonds is greater than the alternative, multiple dangling bonds, and the material will generate defects to lower its free energy. The particular flavor of defects are line defects: edge type, screw type, and mixed type. As soon as these defects depart from the interface and move vertically through an epitaxially grown layer they can be generally referred to as threading dislocation. In semiconductors, nearly all defects will act as recombination centers and scattering centers that will negatively impact device performance.

Another major challenge is rooted in chemistry and thermodynamics. There are two problems here, one is achieving mixing of indium and gallium which have a tendency to drive towards separation. The other is how to supply reactive nitrogen to the surface of the crystal where growth is occurring. The crystal growth temperature plays the lead role in solving these issues, but the whole story comes from the flux and species type of the incident gallium, indium, and nitrogen species.

The chemistry issue with cation mixing of indium and gallium as metals is that they tend not to mix. This carries forward into the nitride compound to create a miscibility gap from about 20% to 80% indium content depending on growth temperature. This has been calculated by Ho et al. and a copy of their phase diagram

is presented in Figure 1.[31] This can create phase separation in layers, causing

separate domains of differing levels of indium. These can create a device with many

competing band gap energies and recombination active regions between them. In

addition, this can create stacking faults in the material which have been theorized to

act as strong recombination centers.[32]
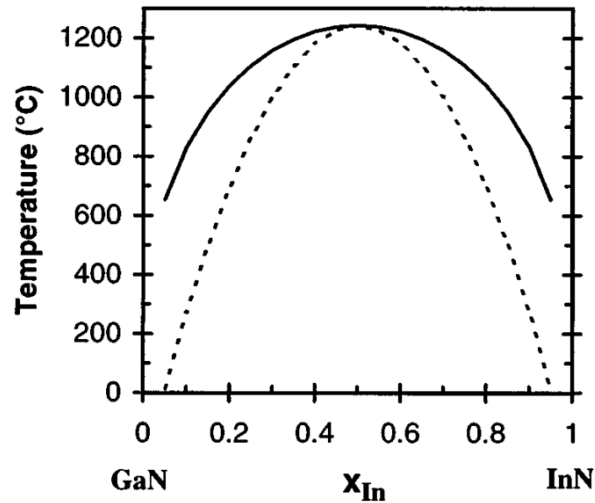
Figure 1. The GaN-InN phase diagram as calculated by Ho et a. "Binodal (solid) and spinodal (dashed) curves for the $Ga_{1-x}In_xN$ system, calculated assuming a constant average value for the solid phase." –I. Ho [31]

As previously mentioned, the other problem with chemistry is the

incorporation of nitrogen into the semiconductor crystal. This is challenging because

though nitrogen makes up ~70% of the Earth's atmosphere, it is in the form of N_2. N_2

is not usable in growth, as it is one of strongest molecular bonds in nature and takes

>2400 °C to thermally crack the molecule into single atoms.[33] Therefore it must

either be pre-cracked using a plasma or come in the form of another molecule. The

ideal molecule for delivering reactive nitrogen is ammonia, NH3. However, even

ammonia requires >450 °C to crack thermally.[34] Broadly speaking, these different

methods of obtaining usable nitrogen for incorporation into a growing crystal are called "nitrogen activation."

These two problems, cation mixing and nitrogen activation, are controlled by temperature, flux, flux ratio, and species type (N^*, NH_3, etc.). However, there are some other issues that can occur within this parameter space in addition to the aforementioned defects. If the nitrogen rate is too high or the surface temperature is too low, then adatom mobility can be greatly reduced and the surface can start to grow in the form of 3-dimensional islands.[35] Another effect of high temperature is that In-N bonds can dissociate preferentially, leading to excess indium on the surface. This is based on the InN decomposition temperature. The temperature at which it occurs scales roughly linearly from the InN to GaN dissociation temperatures.[36]

All of the aforementioned problems contribute to one final challenge, doping. The doping in GaN and InGaN is something known as unintentional doping (UID). This means that without any extrinsic dopants added to the chemistry the material tends to be naturally n-type. Many of the above-mentioned defects contribute to the natural n-type background.[37], [38] This is very problematic for creation of p-type material and the subsequent devices requiring p-type. This problem gets worse as the mole fraction of indium is increased, not only because of the added defects but also due to InN being even more intrinsically n-type then GaN.

The main dopants identified for the III-nitride materials are silicon for n-type, and magnesium for p-type. Both of these dopants are substitutional for the cation lattice site. The ionization energies for these Si and Mg in GaN are roughly 12-37 meV[39] and 135-200 meV (135 meV[40], 155-165 meV[41], 166 meV[42], 170 meV[43], 160-200 meV[44]), respectively. This means the p-type magnesium

dopant, needed for n-type compensation, has a lower probability of thermally ionizing and contributing to the doping level. In order to account for this more magnesium must be added to the crystal. An additional issue with magnesium doping is the formation of a Mg-H complex in the presence of hydrogen such as is created by organics in MOVPE reactors. This however can be treated with a thermal anneal, and this process is referred to as magnesium activation.[45]

III-NITRIDE SOLAR CELLS

Indium-gallium-nitride is of interest to be used as a next generation material to build solar cells. This is due predominantly to its widely tunable band gap and very strong absorption. Additional, desire for InGaN solar cells is generated by the compounds aforementioned high thermal stability and previously unmentioned property of radiation resistance (a useful property for the space PV community). Though these concepts seem alluring for photovoltaic devices, the drawbacks with producing what might be called "solar quality" InGaN material are numerous enough to have prevented significant advancements. These drawbacks are challenges that effect on different solar cell metrics in various ways, and shall be reviewed. The main performance metrics of any given solar cell are open circuit voltage (V_{OC}), short circuit current density (J_{SC}), and fill factor (FF).

The first metric and arguably the most important one of any solar cell is the V_{OC}. Relative to a solar cell the open circuit voltage (the non-zero voltage at zero current) is the maximum voltage achievable under illumination. All else being equal, more voltage is preferable to more current as more of the energy can be used with less series resistance loss. In any device the V_{OC} will always be equal to the material band

gap minus some value. This value is termed the band gap voltage offset, W_{OC}, and for most solar cells equals ~0.4 eV.[46] This metric allows for cells of different technology and band gap to be approximately compared. As material quality starts to effect the V_{OC}, the W_{OC} will get larger. In this way the W_{OC} can be a summary of the imperfections in a solar cell. For the InGaN system, major V_{OC} losses begin to show as the mole fraction of indium rises over 15% or as the InGaN layers exceed their critical thickness and begin to relax. Both of these end with the same issue for V_{OC}, defects. The presence of defects creates recombination centers which reduces the carrier population. As the maximum carrier population is decreased the overall voltage is decreased. Additionally, it is theorized that threading dislocations can act as shunting pathways reducing the V_{OC}.[47], [48]

The next most important metric is the short circuit current or current density, the non-zero current when voltage is equal to zero. —Often these two terms are both referred to as current (incorrectly but manageably) for convenience, though current density is actually used to normalize cells relative to their area. — The J_{SC} can vary greatly relative to the band gap and thus indium composition. This is because as the band gap narrows the required photon energy for the photoelectric effect decreases and an increasing fraction of the solar spectrum meet this requirement. The flip side of this is that the maximum theoretical V_{OC} for a device will be lower. However, this is the internal current or the generation current J_G. This current is not the current that will make it to the wires attached to the solar cell; many of the defects will take away from J_G before it can become J_{SC}. Defects in the form of stacking faults and threading dislocations will directly take away from the current as they will act as recombination centers. Should the device be a heterojunction design, the previously

mentioned polarization effects will create band spikes, blocking a portion of the current. This can be as detrimental if not more so than the defects. Finally, though InGaN has extraordinarily high absorption, using a multiple quantum well approach such as in LED's has difficulty generating thick enough material to absorb the majority of the solar spectrum. These quantum wells also act as traps from which carriers need thermal energy to escape.

The fill factor for a solar cell is a net product of shunt resistance and series resistance. Series resistance, in which lower is better, is largely a product of carrier mobility and device design. While electrons might have good mobility in GaN and InGaN, holes on the other hand have very low mobilities leading to higher series resistance. Higher series resistance will lower the slope of the I-V curve where it intersects at V_{OC}. Shunt resistance on the other hand represents the slope where the I-V curve intersects with J_{SC}, and better shunt resistances tends towards infinity. As shunt resistance is decreased by threading dislocations and recombination centers, this slope will increase. The net result of detrimental effects to each of these resistance types is an I-V curve with less of a box shape and more of a straight line, reducing the operating efficiency of a device despite strong V_{OC} and J_{SC}.
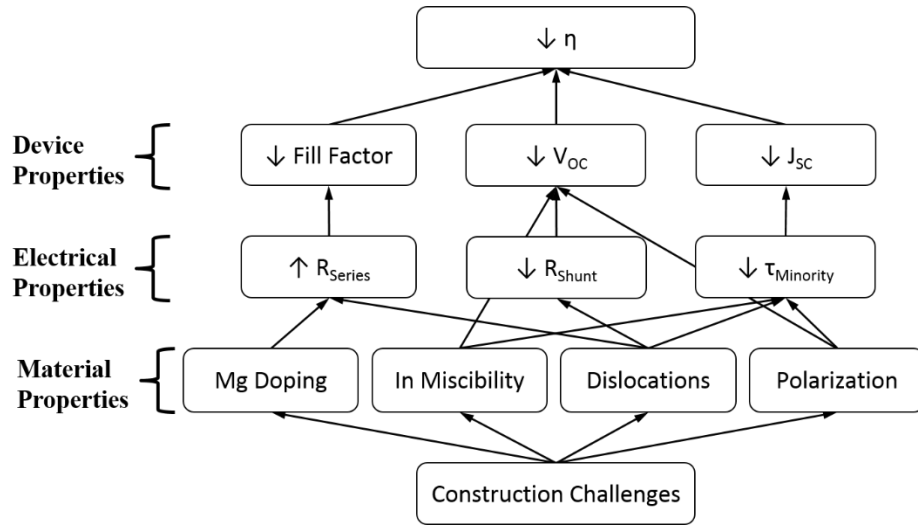
Figure 2. This chart, modified from Bhuiyan et al., shows the challenges associated with materials and device productions. "Schematic representation of the important challenges toward the fabrication of high-efficiency InGaN solar cells and their influences on limiting the performance parameters." - A Bhuiyan[49]

Efforts have been made by many research groups over the years to try to mitigate these problems, or to attempt fabrication of a device in spite of the known issues. In general, efforts have been made by metal organic vapor phase epitaxy reactors (MOVPE) or by molecular beam epitaxy reactors (MBE). The later has the advantage of better layer, flux, and temperature control; while the former has the motivators of throughput and established industrial infrastructure. On both sides, efforts have been made to grow heterojunctions or homojunctions of InGaN solar cells.

INGAN PHOTOVOLTAICS: A STATE-OF-THE-ART REVIEW

InGaN PV devices have been created in a variety of configurations: homojunctions, heterojunctions, p-n, p-i-n, MQW, and SL type devices. Additionally, devices grown by MBE and MOVPE that have demonstrated comparable results. Devices have been grown with varying compositions of indium such that their band gaps are quite different. This makes comparing devices somewhat challenging. A

further complication of comparing previous results is that different cells have been tested under different illumination sources, some sources being 1-Sun while others are monochromatic light, or even UV-enhanced sunlight. In all cases the devices V_{OC} will be quoted, but furthermore the materials W_{OC} will be quoted as that is a better metric for comparing performances of devices with different band gaps. Additionally, when tested under 1-Sun conditions the quantum conversion (QC) (the ratio of J_{SC} to above band gap photons assuming a QE of 1) will be quoted.

The InGaN material system first became of interest for constructing a photovoltaic device in 2003[12], [13], [17], [50] when the InN band gap was revised, however it was several years afterwards that devices in were first made. The first InGaN PV devices were constructed by Jani et al and Yang et al in 2007.[51]–[53] These preliminary cells were built using homojunctions of InGaN and in one case a p-i-n device with absorber InGaN as a faux intrinsic layer sandwiched between p and n GaN regions. Yang et al created a pure InGaN p-n homo junction with contacts directly to the InGaN layers. This device demonstrated both low current density and low V_{OC}. The light source for the I-V curve was monochromatic 360 nm light so it is impossible to rationalize the 0.034 mA/cm^2 short circuit current density relative to a solar spectrum. The W_{OC} for this device was ~2.3 V leaving lots of room for improvement.[53] Meanwhile Jani's two devices (the first p-Gan/i-InGaN/n-GaN and the second p-GaN/p-InGaN/n-InGaN) were reported to have band gaps of 3.2 and 2.5 eV, respectively. These two samples had V_{OC} values of 2.3 V and 2.1 V with corresponding W_{OC} values of 0.9 V and 0.4 V.[51], [52] The later of these would be in accordance with commercial grade solar cells, and therefore may have been slightly optimistic for a technology in its infancy.

Since then the research has grown moderately, and to date there have been roughly 70-100 published InGaN solar devices across approximately 30 different papers. Almost all of these devices are grown on GaN buffers or templates on sapphire with a limited number on more expensive native GaN substrates. Nearly every device is a mesa structure, as demonstrated in Figure 3, with either pn InGaN homojunctions or increasingly more common p-i-n GaN-InGaN-GaN heterojunctions. In the later, the intrinsic region consists of either intrinsic InGaN or InGaN/GaN well/barrier MQW. For these cells the indium percentages in the active absorber ranges from 2%[54] up to 54% [55] and all compositions in between. While in many cases [52], [56]–[60] the W_{OC} is low enough to be close to the 0.4 V rule of thumb, the quantum conversion only once [61] reaches 50% which is far lower than record silicon (96%) and GaAs (93%). [62] Furthermore, there are many cells which achieve neither a high voltage nor a high quantum conversion.
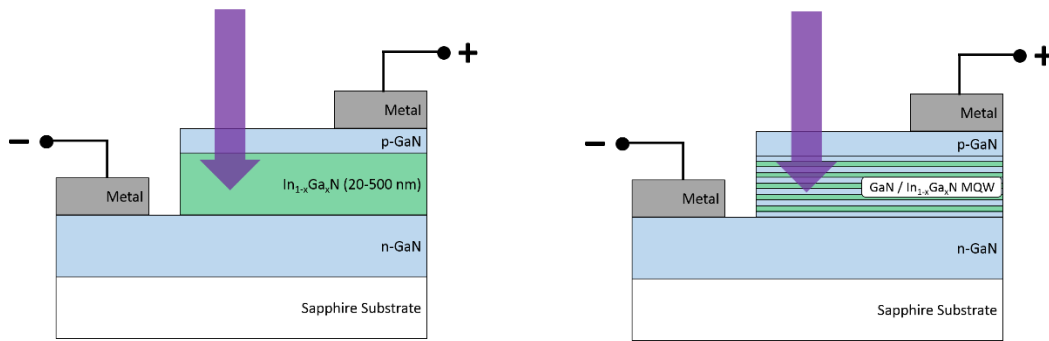
*Figure 3.*GaN-InGaN-GaN device mesa-structures. The device on the left shows a bulk InGaN absorber. The right side shows a GaN/InGaN MQW absorber.

These structures are fabricated on mesas, as previously mentioned. This requires photolithography, etching, and metallization. Common metals are laminar stacks of some combination of Ni, Au, Al, and Ti with some cases also using Cr or Pt. Mesa structures require lateral transmission out of the base. This combined with the

fact that less defective material must be grown first to minimize defect propagation results in the conclusion that the base layer be the higher conductivity lower defect density n-type GaN. Leading to p-GaN as the top emitter, which still requires lateral transport to contact fingers. Unfortunately, p-GaN has significantly worse conductivity than n-GaN.[63] For this reason many groups used a thin (<10 nm) semitransparent metal current spreading layer on top of their p-GaN. [51], [52], [54], [56], [59], [60], [64]–[66] Recently, more work is shifting to use of ITO as a better transparent current spreading layer. [57], [58], [67]–[69] Regardless, current density and thus quantum conversion continue to remain low in InGaN devices whether due to a lack of absorption or a lack of extraction.

As can be seen from this work, attempting to make an InGaN device within the same parameter space as these efforts would likely be an exercise in futility. In order to hope for a breakthrough, a breakthrough must first be made in either the realm of material growth, or a new design for a device capable of operating regardless of these challenges.

This thesis seeks to motivate those ideas. The next chapter, Chapter 2, will describe a new method of delivering active nitrogen to the growth front of crystals. This method uses a modified MBE with a nitrogen source christened 'ENABLE'. Then application of this technique to developing new devices will be explored in Chapters 3 and 4. Upon determining that, new devices are intriguing but material quality limit, subsequent chapters will go back to improvements in material development: buffer layer technology (Chapter 5), high quality InN (Chapter 6) and high growth rate gallium-nitride (Chapter 6). Finally, Chapter 8 will detail the development and testing of solar cells for refractory applications.

18

CHAPTER 2

ENABLE GROWTH TECHNOLOGY

III-N film growths were executed in a custom built molecular beam epitaxy reactor at Los Alamos National Laboratory. This chamber features thermal evaporators for group III elements, in-situ diagnostics, a six-axis sample holder/manipulator, and a custom built nitrogen source. The main chamber is rectangular in shape and sealed with mostly metal flanges. The main chamber is pumped by two large (~2000 liter per minute) turbo molecular pumps backed by standard mechanical rough pumps. A loadlock chamber is pumped by a smaller turbo pump and dry rough pump. The loadlock can cycle between ambient pressure and $1x10^{-7}$ Torr in ~ 1 hour with $1x10^{-8}$ Torr as an ultimate pressure after several days pumping. Additionally, an auxiliary chamber exists which contains diagnostics for the system and nitrogen source.

The state of the chamber is strong. This is determined through various forms of in-situ diagnostic methods: pressure sensors, residual gas analyzers, and thermocouples. All of these are useful with or without a sample loaded. These is also an additional diagnostic tool on the growth chamber used for monitoring the sample: a reflection high energy electron diffraction system (RHEED). Using these tools, various aspects of temperature, chemical composition (of the vacuum or growth surface), pressure, and samples chemical and crystallographic structure can be measured or inferred.

Low vacuum gauges are in the form of convectron gauges, while high vacuum gauges are ion gauges. Convectron gauges work by measuring the heat transferred from a hot filament to a thermocouple in a closed setup, this gives them a working

range from atmosphere down to 1×10^{-3} Torr with a slower response at their lower limit. Meanwhile ion gauges work by ionizing the relatively low number of gas particles using an emitted electron current and then attracting the ionized species. This method requires a low pressure initially but can work to ultra-high vacuum levels, 1×10^{-4} to 1×10^{-12} Torr.

A residual gas analyzer (RGA) is a specific type of mass spectrometer used to measure the quantities of individual species of specific gases when at low pressure, usually below 1×10^{-4} Torr total pressure. This is done by introducing a beam of ionized gas (representative of the system) into a pathway along four cylinders. As these cylinders are cycled sequentially between positive and negative voltage at radio frequencies, the ions move forward in a spiraling motion based on the voltage, frequency, and their mass. Only ions of the selected mass will make it to the far end of the columns where their charge is measured in a Faraday cup. This works well at selecting specific masses but has the drawback that there can be misleading signals. For example, N_2 and CO both have a mass of 28, so both would be counted towards the signal for mass 28. This is known as isobaric interference. Overall, the precision and fast sampling rate of an RGA far outweigh the inherent issues and make it an invaluable diagnostic tool. Other important uses for the RGA will be discussed during methods of sample growth.

The final aspect of in-situ diagnostics within the growth chamber is the RHEED system. This employs an electron gun and electron phosphorescent screen coupled to a camera. Both the gun and the screen are mounted opposite each other on either side of the sample holder. The electron gun delivers a beam of electrons (several microamps with 20 KeV of energy) towards the surface of the sample at a glancing

angle. The electrons will interact with the surface of the sample, and if the surface is crystalline and oriented properly the electrons will diffract. The pattern of their diffraction will appear on the phosphorescent screen, which in turn is captured by the camera to be sent to the RHEED system software. Diffraction patterns are representative of the top surface (<2 nm depth) of the sample. Streaky patterns are indicative of two-dimensional growth, and result from a lack of deconstructive interference in one direction (direction blocked by the sample). Spotted diffraction patterns, similar to those of a transmission electron microscope, indicate that samples are growing three dimensionally due to complete constructive and deconstructive interference in all directions.

Metal evaporators in the chamber consist of SUMO effusion cells for Al, Ga, and In; a single heat source cone crucible for Mg; and rod in pocket type e-beam evaporator for Nb. As the chamber is constructed in the form of a box, the evaporator sources are suspended on posts from the floor or ceiling of the chamber so that they may be at adequate distances and angles with respect to the wafer surface. The Veeco SUMO cells contain tubular shaped crucibles constructed from pyrolytic boron nitride. The opening on the crucible is narrower than the interior of the crucible. This restricts gaseous metal evaporated from the source material and creates a pressure gradient across the crucible aperture. Thus creating a virtual point source located at the opening of the crucible which creates a stable and uniform flux at the wafer surface.[70] The conical Knudsen evaporator for magnesium doesn't have this crucible design, as a result the flux is less stable. Additionally, evaporation of magnesium can be challenging.[71]

The ENABLE source is the unique aspect of this growth chamber, and it is fairly complex compared to most other sources. It consists of several different components that will all be discussed: the laser, the gas manifold, the source chamber, and the differential pumping. These work together to create a collimated beam of neutral atoms with kinetic energies that is unlike anything on the market. The beam largely consists of a carrier noble gas and a seed of reactant species, i.e. argon and nitrogen atoms.

The gas mixture that is representative of the final beam mixture is provided using a gas manifold. This gas manifold consists of four mass-flow-controllers (MFCs), with precision in standard cubic centimeters (sccm). The gases suppled to these MFCs come through purged gas lines from gas purifiers and from bottled gases of ultra-high purity. The common gases provided through this manifold are Ar, N_2, and O_2 with two MFCs controlling the N_2 flows. Of these two, one has 1 SCCM precision and the other has 10 SCCM precision with upper limits of 500 SCCM and 5,000 SCCM, respectively. The O_2 source stream is used for unassociated projects in the chamber. This source stream can also be easily swapped for other gas sources, most notably other elements of noble gases. Gas lines are stainless steel and fitted with Swagelok seals to prevent contamination from atmosphere. Between the gas manifold and the ENABLE source chamber there exists a pressure gauge (assumed to be representative of the pressure within the source chamber) and valve to a vacuum line to purge the gas manifold to source line.

The laser used in the ENABLE source is a continuous wavelength (CW) carbon dioxide based laser with a power rating of 3500 Watts at 100%. The beam path for this laser from the cavity to the source chamber is encased within an interlocked

enclosure which has a positive pressure of dry air to maintain beam stability. The laser enters the source chamber through a ZnSe window in combination with a ZnSe refractive lens. An additional pulsed CO_2 laser is directed into the source chamber through the same final beam path as the main CW laser. This pulsed laser is used to supply the activation energy for igniting the plasma within the chamber.

The source chamber is the truly custom built piece of the ENABLE source. It consists of a cylindrical volume several centimeters in diameter and several centimeters long. On one end of the chamber there is the ZnSe lens and on the other end there is a supersonic nozzle. The walls of the chamber contain several ports for the inlet of gas flow from the manifold, as well as ports for releasing extra pressure. The pressure release is needed because the source gas flow serves as cooling for components in the chamber in addition to becoming part of the beam. Therefore, the excess gas that is not desired to increase the flux of the beam, will go out the exhaust line. There exists an MFC on this line as a way to regulate the exhaust and thus regulate the pressure in the chamber, an important parameter for stabilizing a plasma.

Two additional design components in the chamber are unique and essential. The first is the lens housing. The percentage of laser power absorbed in the lens as a percentage is relatively low (<2%), but that means it still absorbs a significant amount of energy absolute. This energy all becomes heat and because of the nature of lenses, the heat generation profile is non-uniform. Non-uniform heating, with subsequent thermal expansion can lead to very short component life times (<60 seconds). To overcome this and thus maintain normal operation, cooling is required. The lens is cooled partially by conduction to housing into which it is set, but furthermore by

convection from the inlet gases. The inlet holes direct the gas mixture across the surface of the lens thus providing the additional cooling needed to keep the piece at a sustainable temperature. Additionally, the lens must be capable of co-axial translation. To achieve this a manual linear actuator with a micrometer is used to move the lens housing in and out. The lens is technically separate from the rest of the chamber. The two are sealed together using a set of three O-rings with two layers of differential pumping between them. This allows the inside of the source chamber to remain at elevated pressure while existing inside a larger vacuum chamber.

The other unique and essential component of the source chamber is the nozzle. The nozzle is by design a supersonic nozzle. The nozzle is cut into a copper flange which is silver soldered into a stainless steel flange that caps the fore end of the source chamber. The materials are chosen for their thermal conductivity, which helps to keep them cool in the presence of all the energy from the laser and subsequently the plasma. To further facilitate cooling there is an interior circular channel cut into the copper section that mates to inlet and outlet lines machined within the steel flange. These cooling lines flow within the overall flange and specifically around the active nozzle region, preventing these metals from deforming or melting. Finally, the entire piece is electroplated with several microns (>2.5 µm) of gold. This layer prevents corrosion in the presence of so many active and energetic ions.

Theoretically this nozzle design will collapse a particle's six-free degrees of motion into one translational degree, thus resulting in elevated kinetic energies. On one side of the nozzle the pressure is around 4-4.5 kilo Torr, while the other side is closer to 100 micro Torr. This pressure drop is substantial, but the team at Los Alamos has empirically determined (unpublished) that it is not enough to produce a useful

beam. Therefore, the plasma not only serves to crack molecular bonds but also to create a virtual pressure at the inlet of the nozzle. Assuming an ideal gas law relation and a several thousand Kelvin plasma temperature, the plasma adds roughly three orders of magnitude to the pressure differential.

The plasma itself is elliptical in nature, relatively small, and located at the focal point of the refractive lens. It is created when the pulsed CO_2 laser adds its energy to the CW laser under elevated pressure (exhaust closed). After which the pressure can be returned to normal operating levels and the CW laser can sustain the plasma. The plasma is approximately several hundred microns in diameter and several millimeters long. By translating the lens in or out of the chamber the plasma can be driven into the nozzle. This gives higher kinetic energies of species in the final beam source but has the disadvantage that it can seriously degrade the lifetime of the nozzle. Furthermore, the tilt of the lens with respect to the alignment of the laser is important, as it can move the plasma into the sidewall of the nozzle. This will quench the plasma causing it to extinguish.

Lifetimes have been mentioned for two main parts for the ENABLE source: the lens and the nozzle. These pieces do wear out and do need to be replaced. However, proper use can elongate their lifetimes and preventative maintenance can avoid unplanned system down time. Roughly speaking the lens costs several hundred dollars, needs to be custom ordered in advance, and gets roughly 300-1000 hours of use. Factors that shorten the lens lifetime are unplanned extinguishings of the plasma and flowing gas mixtures with lower thermal conductivity. The nozzle will last considerably longer, approximately ten-fold the life of a lens. Life spans for a nozzle are several years with the main factor shortening life being how far into the nozzle

the plasma is positioned. This is good as the nozzle costs approximately an order of magnitude more than the lenses.

The jet of supersonic expansion that comes out of the nozzle is a ballistic mixture of ions, radicals, electrons, and atoms. To condition the beam, and keep background pressures in the main chamber low, the beam passes first through a skimmer cone. Then the beam passes through two layers of differential pumping separated by apertures. The result is a well-collimated beam that is mostly atomic. This is due to coulombic forces either repelling ions out of the beam before one of the apertures, or aiding in electron-ion recombination.

If the nature of this description seems very qualitative, that is because it is. By design, the dispersion of knowledge about the source chamber specifics has been limited. Therefore, what has been presented above is to the best knowledge of the author. The schematic below is crude guide to the general setup for the beam.
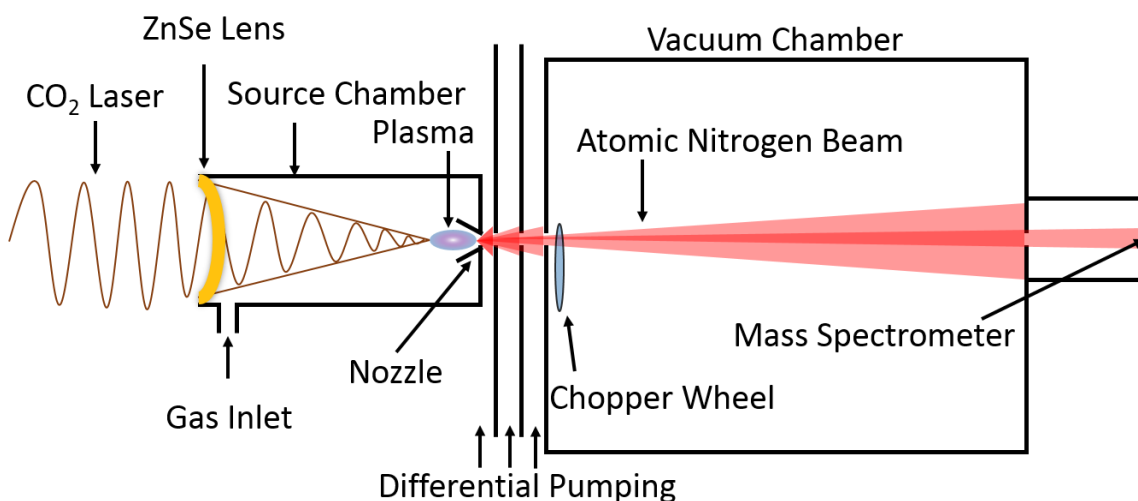
Figure 4. ENABLE source cross-sectional schematic detailing positioning of components described in the chapter above.

CHAPTER 3

LOW TEMPERATURE GALLIUM NITRIDE ON SILICON

The advent of the silicon HIT (heterointerface with thin intrinsic layer) cell from Sanyo[72] (now Panasonic) as a record setting[73] solar technology has spurred a great deal of interest in thin film passivation technologies and heterojunction technologies for commercially abundant silicon wafers. Work has been done to understand and ultimately duplicate the HIT cells technology.[74]–[78] Furthermore, many are trying to improve the technology by improving or replacing the a-Si layer, indium-tin oxide layer (ITO), or both.[79]–[84]

The search for new materials that can replace a-Si and/or ITO will provide a clear pathway to higher efficiency Si devices.[80] Currently, one of the largest loss mechanisms in these HIT cells is parasitic absorption of the solar spectrum in layers above the active absorber, the silicon wafer. It has been shown that free carrier absorption in ITO and band-band absorption in a-Si accounts for a loss of $2.5 mA/cm^2$.[76] Therefore replacing these material with a different material capable of the same transport and passivation functions but with significantly increased transmission of the solar spectrum should result in better device performance.[80]

Potential candidates for new carrier selective contacts (CSC) on silicon should have conductivity comparable to ITO, optical transmission greater than either the ITO or the a-Si being replaced, and should have sufficient passivation to enable long carrier lifetimes (≥ 500 µs). Passivation in these Si devices is largely a function of the band alignments at a heterointerface. These band alignments can be predicted through use of the Anderson model approximation of band alignments.[85]

27

GaN, among others, has been predicted as a speculative candidate for use as a CSC on Si.[80] At room temperature GaN can easily achieve electron mobilities ≥ 1000 cm^2/V-s, at room temperature with dopant concentrations of 10^{19} /cm^3 resulting in conductivity of at least 1600 1/Ω-cm.[23] Such a conductivity should be comparable with industry standard TCO's ~5000 1/Ω-cm.[86] Absorption of the solar spectrum by GaN is nearly zero; with a band gap of EG=3.44 eV it threatens to parasitically absorb up to 0.5 mA/cm^2 (0.77%) of the solar photon current. This is much lower than the parasitic absorption due to TCO and ITO.

The effectiveness of GaN as a CSC for silicon can be approximated from an analysis of the band diagram. The Anderson model[85], [87], [88] of heterointerfaces is applied to the band alignment of GaN-Si and the results are demonstrated in Figure 5. This band model is produced using the following band alignment properties E_G^{Si}=1.12 eV, χ^{Si}=4.05 eV, E_G^{GaN}=3.4 eV, and χ^{GaN}=4.1 eV.[89]–[91] This prediction shows a strong preference for GaN to act as an electron selective contact. Likely, the number of dangling bonds at the interface will be the high due to the degree of epitaxial mismatch. It is possible that in spite of this the spontaneous polarization of the GaN crystal would passivate this interface. Alternatively, GaN can be used in conjunction with a thin layer of a-Si to investigate the possibility of GaN as a replacement for only the ITO.
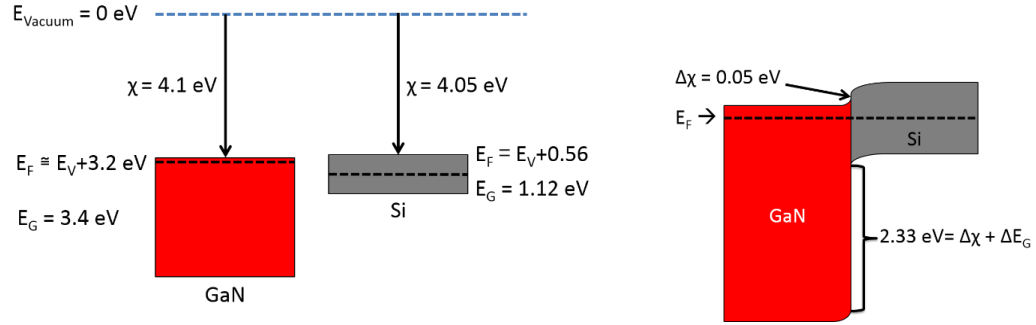
Figure 5. Schematic of GaN and Si band alignments. *Figure 5*a) on the left shows all relevant energy levels referenced to the vacuum level. *Figure 5*b) on the right shows an Anderson model approximation of band alignments.

CHARACTERIZATION OF GAN ON SILICON

Preliminary investigations of the use of GaN on Si for CSCs is presented here. Samples involved a number of permutations: wafer compound, wafer growth, wafer orientation, a thin a-Si layer, growth temperature, nitridation of the surface, and duration of growth. Wafer were Czochralski (CZ) silicon (110), CZ silicon (100), float zone (FZ) silicon (100), or sapphire (0001). These and the remainder of the permutations are shown in Table 2.

Samples were prepared either solely in the ENABLE system or first in the PECVD followed by the ENABLE system. For samples with a-Si growth temperatures were kept at or below 200 °C to avoid compromising the a:Si electrical properties. During preparation sample crystal structures were characterized using RHEED. Corresponding RHEED measurements can be seen in Figure 6. RHEED patterns were used as first approximation of structural nature. These show that a-Si samples without nitridation have a strong tendency towards very weakly oriented mostly polycrystalline growth. Meanwhile identical films that had no a-Si but had nitridation showed oriented though weakly diffracting patterns. Weak and broad peaks are attributed to imperfect crystal formation due to low adatom mobility as a result of low

temperature. Additionally, six fold peak orientation may indicate the formation of a zinc-blende phase.[92] The additional two patterns exemplify effects of a better suited substrate and higher growth temperature with better defined streaks and stronger signal to noise ratio.

Table 2
Growth Conditions of GaN on Silicon

Sample No.	Wafer	Wafer Growth	Growth Temp.	a-Si	Nitridized	Growth Time (s)	T @ 10^{15} cm^{-3} in air (μs)	T @ 10^{15} cm^{-3} in HF (μs)
1027	Si (110)	CZ	700°C	no	yes	600	1.7	0.8
1028	Si (110)	CZ	500°C	no	yes	600	1.9	2.3
1029	Si (110)	CZ	300°C	no	yes	600	2.7	1.9
1030	Si (110)	CZ	80°C	no	yes	600	2.9	2.1
1035	Si (100)	CZ	700°C	no	yes	1200	3.3	1.3
1057	Si (100)	FZ	200°C	no	no	360	3.4	47
1060	Si (100)	FZ	200°C	yes	yes	360	5300	5200
1061	Si (100)	FZ	200°C	yes	no	360	4000	4700
1062	Si (100)	FZ	200°C	no	yes	360	4.6	52
1068	α-Al$_2$O$_3$ (0001)	FZ	200°C	no	yes	360	N/A	N/A
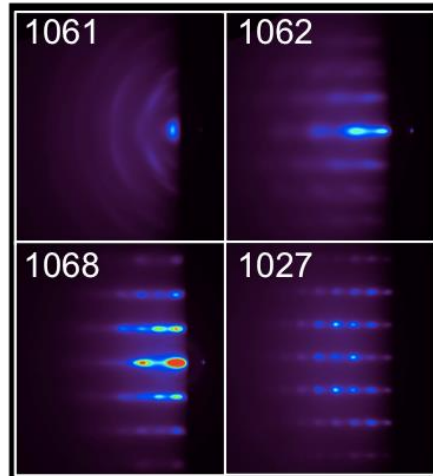
Figure 6. RHEED patterns of GaN surface post growth. 1061 shows polycrystalline nature with weak ordering. 1062 depicts zinc blende GaN. 1068 of GaN on sapphire is a reference for more the more typical. The spotted streaks in 1027 are indicative of three dimensional film growth. 1068 and 1027 show wurtzite diffraction patterns.

XRD measurements were performed to quantify the crystal quality of the GaN layer. Wide range ω-2θ scans of samples are shown in Figure 7, Figure 8, Figure 9. These diffraction patterns show that the GaN layers are oriented with their c-axis perpendicular to the surface, i.e. not fully polycrystalline. This is shown by the absence of any peaks besides the GaN (0002) and (0004) peaks. The wide full width

31

half maximum of the peaks makes it impossible to discern any cubic phase from the hexagonal phase, since the (0002) wurtzite peaks is theoretically at 2θ=34.56° and the (111) zinc-blende phase is at 2θ =34.46°.
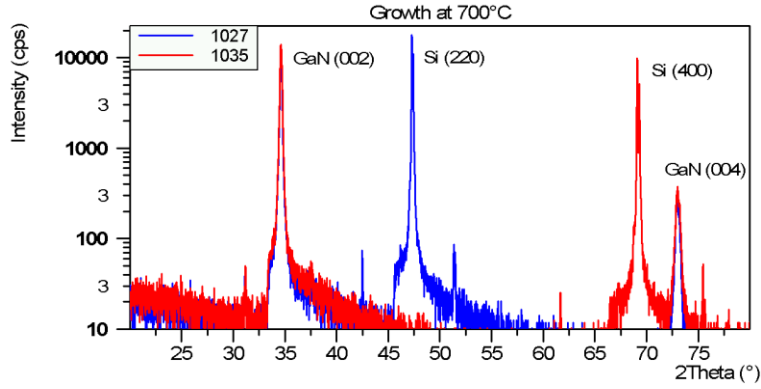
Figure 7. ω-2θ X-ray diffraction pattern are from GaN growths at 700°C on (110) and (100) oriented Si substrates. Diffraction peaks from the Si substrate and GaN film are labeled. Small peaks are artifacts of the measurement
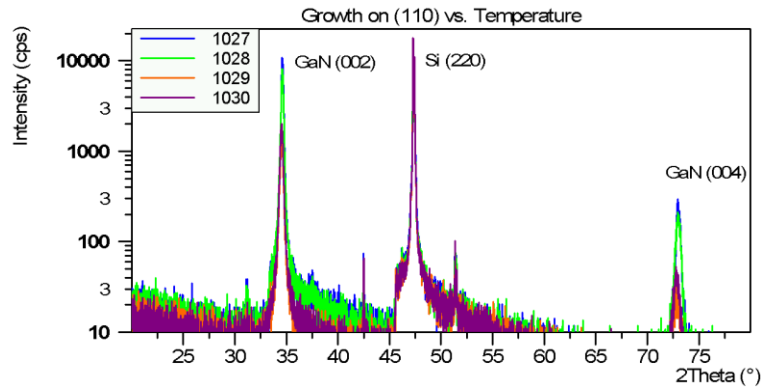
Figure 8. ω-2θ X-ray diffraction patterns of four different films each with different growth temperatures. Intensities are all within an order of magnitude but decrease with decreasing growth temperature, and non c-axis oriented crystals are not present. Small peaks are artifacts of the measurement.
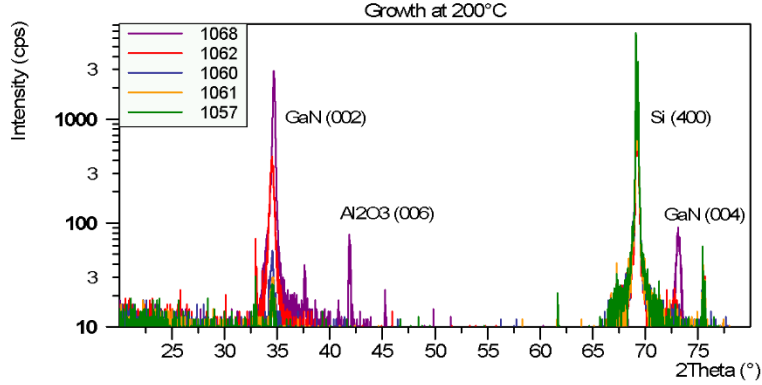
Figure 9. ω-2θ X-ray diffraction patterns of five different films all grown at 200 °C. Only growth on the sapphire substrate shows a GaN (004) peak, indicative of the superior crystal quality of growing on sapphire vs. silicon. The second strongest intensity comes from 1062 which was a nitridized bare wafer. Subsequent films are very weak in intensity, which agrees strongly with the poor RHEED diffraction patterns. Small peaks are artifacts of the measurement.

Samples have been optically measured by VASE, spectrophotometry, and lifetime flash tester. Fitting of the VASE data estimates the thickness of the 360 sec growth at 95-100 nm. This gives a growth rate of ~16 nm/min which is in good agreement with other GaN growth rates on this system at significantly higher temperature. Therefore the adatom sticking coefficient is nearly unity (or shows no change) from 800 °C down. VASE data can also be interpreted to give the absorption coefficient. This is plotted in Figure 10. The band edge for the GaN on Si samples is about 40 nm lower compared to the GaN on sapphire sample. This band gap narrowing is likely due to poor crystal quality. In general, the absorption for the GaN is all at shorter wavelengths than that present in the solar spectrum (roughly 1.3 mA/cm^2).
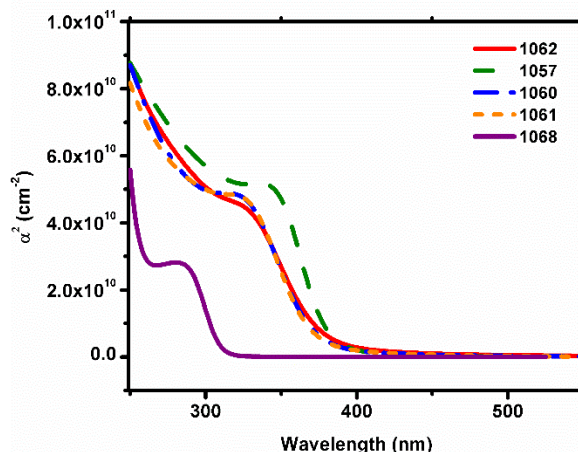
Figure 10. The square of the absorption coefficient vs. wavelength. For almost all films the absorption is in the UV. None of these low temperature films exhibit an intrinsic band-edge of 365 nm.

Lifetime measurements of a control sample with a-Si on both sides of a Si wafer resulted in long carrier lifetimes (τ_{eff}=757 µs) indicating strong passivation of the surfaces and yielding an implied V_{OC} of 668 mV. Measurements from samples with GaN directly on a Si wafer results in short carrier lifetimes (τ_{eff} = 54 µs, $ImpV_{OC}$ = 551 mV) indicating that the surface is not effectively passivated by GaN alone. Finally, the deposition of GaN onto an a-Si passivation layer does not significantly decrease the lifetime from the a-Si only sample (τ_{eff} = 646 µs, $ImpV_{OC}$ = 664 mV). This result is promising for the further development of this field.

CHAPTER CONCLUSION

The use of GaN as an electron selective contact to improve the performance of HIT cell has shown some interesting preliminary results. These films have shown unexpected preferential orientation to wurtzite c-axis. Optical values indicate that low temperature GaN still has a bandgap high enough to not incur parasitic absorption of the solar spectrum. Lifetimes are affected by growth of the GaN directly

on the Si substrates, but are unaffected by growth when GaN is deposited on a-Si on the substrate. This leads to the possibility of using GaN for a CSC and transparent conducting layer while still utilizing undoped a-silicon for interface passivation. Further experiments are needed to investigate and verify assumptions about electrical properties of GaN grown under these atypical conditions. Also, further research into GaN polarity and the Si-GaN interface may yet be able to yield a passivation comparable to that of a-Si.

CHAPTER 4

INVERSION JUNCTIONS AND $IN_{1-X}GA_XN$

The most popular area of research for III-N materials in solar cells is the development of junctions with band gaps relevant for multijunction tandem cells. Current multijunction technology consists of 3 and 4 junction cells with average efficiencies around 40% and a champion world record efficiency of ~46%, both under concentration. Despite these astounding efficiencies (roughly twice that of silicon technologies), this technology is facing an uphill battle in the industry because the LCOE (levelized cost of electricity) is only marginally better than silicon in the only most favorable of locations (geographies with low cloud cover). The best way to decrease the LCOE is to increase the efficiency of the cell. The clearest roadmap to increasing cell efficiency is to add junctions to the stack, with the biggest need for material development in the high band gaps. These are band gaps where the use of InGaN starts to make sense as a junction material. Table 3 shows the band gaps and equivalent InGaN compositions for different tandem devices.

Table 3
EG and associated Indium % for Detailed Balance Junctions

Junction ID	Top Junction of 5	Top 2 Junctions of 6	Top Junction of 6
Ideal E_G	2.1 eV	1.7 eV	2.3 eV
Indium %	~38%	~52%	~32%

The band gaps needed for these devices all exist within the challenge region of InGaN, and thus have considerable materials limitations for solar. These materials are difficult to grow without phase separation leading to band gap fluctuations and defect regions creating a myriad of recombination centers. These defects also tend to

be of the electron donor variety, thus making p-doping of the material increasingly difficult. Furthermore, thermodynamics makes maintaining proper surface conditions for mixing and incorporation of indium and gallium difficult, and it makes mixing and incorporation of indium, gallium, and magnesium (p-type dopant) nearly impossible.

While heavy magnesium doping of GaN has been achieved, very little experimental work has shown successful p-type doping of InGaN. Gunning et al. have demonstrated very good p-type doping of gallium nitride by creating an impurity band of magnesium. This technique has been shown to significantly reduce the activation energy of holes in GaN from ~120 meV to 40 meV.[93] However, very little has been done to create similar results in InGaN.

These results are problematic for building a homojunction InGaN device, but in a heterojunction it would be less of an issue. However, a standard heterojunction, is not suitable for lower band gap InGaN solar cells since the spontaneous and piezoelectric polarizations create device limiting band spikes, that prevent current collection under light bias near the maximum power point.[94], [95]

We have proposed an inversion junction device, which will use the polarization effects to invert a region of the n-type material to create a thin effective p-type region.[96] The inversion junction (previously called "induced junction") is created when electric fields from electrostatic or polarization effects strongly bend the bands of an active material and invert the surface.[74] This means that with respect to the Fermi level an n-type material will appear to be locally p-type. A schematic of such a band diagram is shown Figure 11. The realization of this design requires control and measurement of the strain and piezoelectric properties, and design of the interface to accommodate both interface inversion and transport across the interface.

37

In this chapter, we present the design, the material requirements, and experimental investigation of materials that can be used to realize an inversion junction solar cell. It has already been shown how band gap requirements and corresponding InGaN compositions allow higher theoretical efficiencies compared to existing materials. "Modelling Methods" presents the modeling of an inversion junction system, taking into account strain, material quality and piezoelectric properties. "Growth and Characterization" presents the growth of InGaN with a large indium mole fraction to achieve band gaps in the 2 eV range, and the analysis of the material and devices.
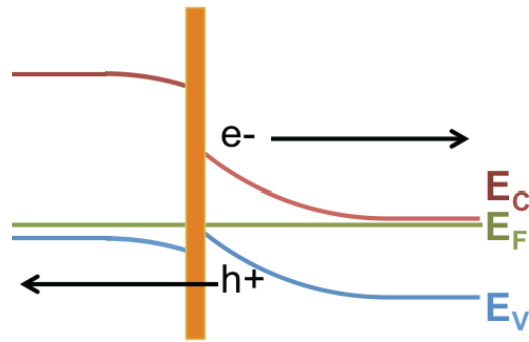
Figure 11. A schematic representation of an inversion junction. The material on the left is a p-type window layer. The layer in the middle is an extremely thin high bandgap material. The material on the right is the absorber and actual inversion junction.

MODELING METHODS

An inversion junction achieves carrier collection by creating a strongly inverted region at the interface of an n-type InGaN layer and another layer. A schematic of the device is shown in Figure 11. InGaN is the only optically active layer; with the other layers being primarily responsible for carrier extraction and influencing the band bending of the InGaN layer. Thus, while the structure appears

similar to a normal heterojunction, its transport and recombination properties are not dependent on the GaN layers (or other high band gap layer).

The operation resembles strongly to that of a minority carrier MIS device used in solar cells. The strong inversion reduces the interface recombination and assists in the overall carrier transport through the i-region and to the top contact by lowering the effective barrier that the carriers encounter at the heterointerface.

It has several advantages over a pn-junction or heterojunction. The absence of the heavily doped emitter results in the elimination of the doping-induced degradation of minority carrier lifetimes. This, in addition to being a thin junction (50 to 100 nm), reduces carrier recombination in the inverted region. Furthermore, the band bending at the interface reduces the effective surface/interface recombination velocity and makes the device less dependent on interface quality, both increasing efficiency and decreasing the material requirements for the high band gap layer.

The analysis of a band diagram at equilibrium provides insightful information about the operation of a device. The equilibrium band diagram for a GaN-AlN-InGaN inversion junction has been simulated with a computer model developed in the commercial simulator package Sentaurus. A few of the important parameters of the model are described below to help better understand the equilibrium band diagram. The InGaN, AlN and GaN layers are 500 nm, 5 nm and 300 nm thick respectively. The fraction of indium content in the $In_xGa_{1-x}N$ layer is x = 0.25. The GaN is p+ doped while the InGaN is n+ doped with effective carrier concentrations of 10^{16} holes/cm3 and 10^{18} electrons/cm^3 respectively. Although, Sentarus is capable of handling piezoelectric polarization internally, the developed model in the present structure does not include strain and stress dependent polarization effects. This shortcoming is

overcome by calculating the piezoelectric charges separately and introducing the calculated charge as a sheet charge at each of the interfaces. The calculations assume fully strained layers. Equations (3)-(10) (at the end of the chapter) used for the calculation of the piezoelectric charges are those reported by Chen et.al.[97]
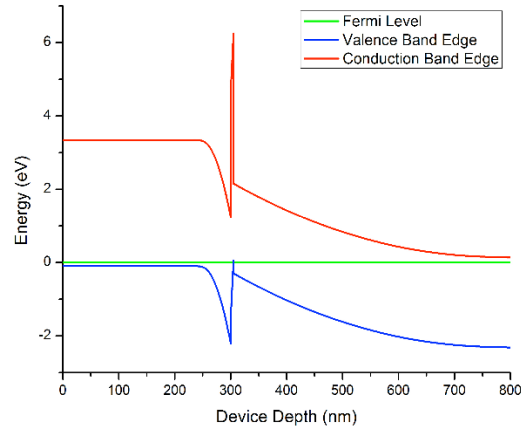
Figure 12. Results from Sentaurus for band alignments of a GaN-AlN-In$_{0.25}$Ga$_{0.75}$N. The device is at equilibrium.

The equilibrium band diagram in Figure 12 shows considerable band bending at the interface between InGaN and AlN. Due to band bending, the concentration of holes in the InGaN at the interface under thermal equilibrium is more than the n-type background doping in the quasi-neutral region. This results in an inversion of the InGaN near the interface. The inversion region assists in the carrier transport mechanism across the heterointerface by lowering the effective barrier that carriers encounter at the heterointerface. The effective barrier is a function of both the band offset that is fixed and the band bending that is a function of applied potential. A lowering of the effective barrier influences both thermionic emission and tunneling transport mechanisms. Modeling performed by Ghosh et. al has demonstrated this effect in crystalline silicon-amorphous silicon interfaces.[75]

GROWTH AND CHARACTERIZATION

In$_x$Ga$_{1-x}$N films were grown to explore the experimental quality and thus feasibility of their use for such devices. Films were grown on bare epi-ready c-plane sapphire substrates. Details on the ENABLE growth conditions have been reported previously.[98]–[100] Substrates were degassed at ~900 °C and pre-nitrided at ~400 °C. Chamber pressures during growth were ~10^{-5} Torr. A quality GaN-In$_x$Ga$_{1-x}$N structure was grown as a control, and a second structure was grown comprised of GaN-AlN-In$_x$Ga$_{1-x}$N both with x=0.25. The structures' growth details are presented in *Table 4.*

Table 4
Sample Growth Parameters

Sample #	Layer #	Description	Nominal Temp.	Thickness
Control Sample "ENB-775"	0	Sapphire Substrate C-plane	N/A	~500 μm
	1	GaN Buffer	750 °C	~300 nm
	2	In$_{0.25}$Ga$_{0.75}$N Buffer	550 °C	~100 nm
	3	In$_{0.25}$Ga$_{0.75}$N	600 °C	~750 nm
"Proposed Device" ENB-746	0	Sapphire Substrate C-plane	N/A	~500 μm
	1	GaN Buffer/Film	800 °C	~300 nm
	2	AlN Thin Film	850 °C	~5 nm
	3	In$_{0.25}$Ga$_{0.75}$N Active Layer	550 °C	~500 nm

Crystal properties of structures were analyzed by high-resolution x-ray diffraction (HRXRD). Photoluminescence was performed to determine the band gap energy. Spectra intensity was calibrated by removing the background and also by considering the quantum efficiency of the PL system. Both techniques were used to determine the degree of compositional splitting. Diffraction patterns of triple-crystal

ω-rocking curve scans are used in conjunction with models developed to estimate defect densities.[101]
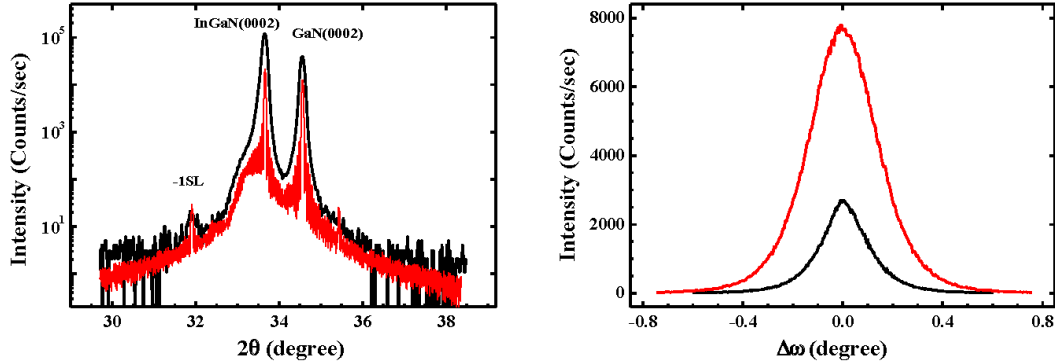
Figure 13. HRXRD of "Control Sample" Left) shows a double crystal 2θ-ω (black – experimental, red – calculated) in the vicinity of InGaN and GaN (0002) reflections. - 1 superlattice peak indicates an unintentional modulation of In composition in InGaN layer with the period ~5.5 nm. The shoulder on the left side of InGaN (0002) peak is related to the small gradient of composition in InGaN layer on the initial stage of deposition. Right) shows a triple crystal ω-scan, measured on the maximum of GaN (0002) (black) and InGaN(0002) (red) peaks. FWHM of these peaks is 740 and 1,140 arc-s, accordingly.

Analysis of 2θ-ω scans on Figure 13 shows the existence of gradients of indium composition in the InGaN film ranging from x≈0.34 to x≈0.26. This is likely related to the InGaN buffer layer grown at a 50 °C temperature difference. There is a super latticing peak that arises from unintended indium composition modulation at the main part of the epitaxial layer. The period of modulation is ~5.25 nm. Also, there is a lack of an InN peak, indicating no In-Ga segregation. The triple-crystal ω-scan indicates defect densities in both the GaN and InGaN layers. The GaN film has a FWHM of 740 arc-sec. This gives a density of dislocation loops ~ 5.6×10^8/cm². The $In_{0.26}Ga_{0.74}N$ film has FWHM of 1,135 arc-sec. This gives a density of dislocation loops ~1.35×10^9/cm². The $In_{0.34}Ga_{0.66}N$ gradient film has FWHM=2,340 arc sec. This gives a density of dislocation loops in this area ~ 5.6×10^9/cm².
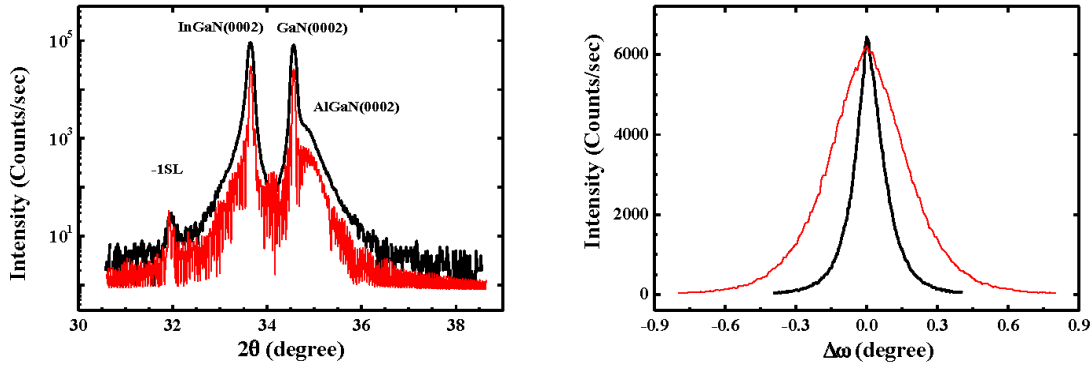
Figure 14. HRXRD of "Device" Sample Left) shows a double crystal 2θ-ω Rocking Curves (black – experimental, red – calculated) in the vicinity of InGaN and GaN (0002) reflections. -1SL peak indicates an unintentional modulation of In composition in InGaN layer with the period ~5.35 nm. The shoulder on the right side of GaN (0002) peak is related to the thin AlGaN layer, created on the top of the GaN buffer layer. Right) shows a triple crystal ω-scan, measured on the maximum of GaN(0002) (black) and InGaN(0002) (red) peaks. FWHM of these peaks is 455 and 1,265 arc-s, accordingly.

The "device" sample shows similar characteristics with respect to indium composition gradient and super latticing modulation spacing, as shown in Figure 14. Values for these are $x \approx 0.26$ to $x \approx 0.32$ and 5.35 nm, respectively. The compositional splitting here could be due to initial stages of growth on the mismatched surface, or increased IR absorption from the heater as the film thickens, increasing the alloy temperature. They also, share a lack of InN phase separation. It appears that the intentional AlN layer is actually an $Al_xGa_{1-x}N$ layer with a compositional gradient from $x \approx 0.33$ to $x \approx 0.05$. The triple-crystal ω-scan shows defect densities in the GaN, AlN, and InGaN layers. The GaN film has FWHM=460 arc-sec. This gives a density of dislocation loops ~ 1.5×10^4 /cm (2.2×10^8 /cm^2). The $In_{0.26}Ga_{0.74}N$ film has FWHM = 1,290 arc sec. This gives a density of dislocation loops ~ 4.1×10^4 /cm (1.7×10^9 /cm^2). The "AlN" film has FWHM = 490 arc-sec. This gives a density of dislocation loops ~ 1.6×10^4 /cm (2.2×10^9 /cm^2).

Photoluminescence (PL) measurements of the samples were performed with a 325 nm wavelength HeCd laser to analyze the band gap for each film, see Figure 15. The PL graphs show films with some compositional variation, which is in agreement with the XRD. These samples show PL peaks at ~580 nm (~2.14 eV) and ~615 nm (~2.08 eV) with some lower intensity peaks at even longer wavelengths. If we assume the compositional certainty of the XRD and use a reported value of 1.36 eV[102] for the bowing parameter, then x≈0.26 to x≈0.32 should give peaks at ~510 nm (~2.51eV) and ~570 nm (~2.24eV) respectively. Thus, it seems that the photoluminescence from these films is red-shifted due to either strain or defects.
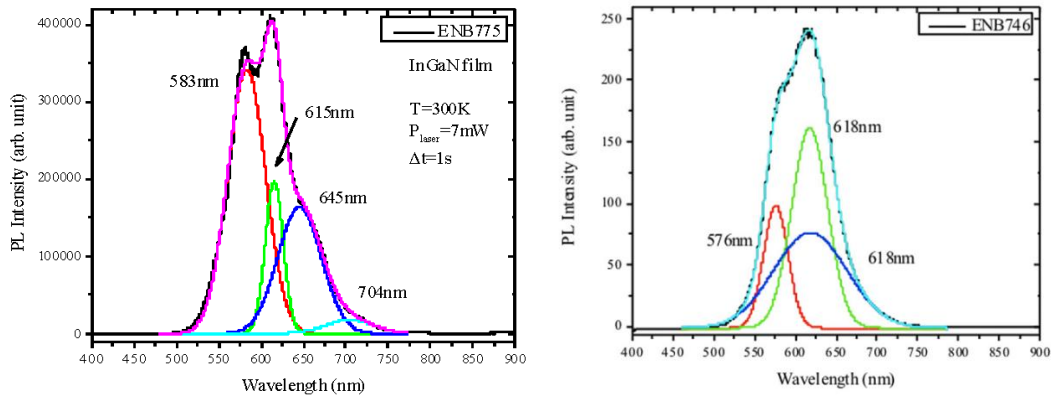
Figure 15. Left) "Control" and Right) "Proposed" show photoluminescence of the InGaN epilayer. Probing laser power of 7 mW. Collection time was 1 second. The black line is the original spectrum. The colored lines are estimated deconvolutions.

In summary, we have modeled the effects of spontaneous polarization and piezoelectric field due to strain as a means for inducing a junction in indium gallium nitride alloys. Experimentally, we have determined that the growth of such films and especially an aluminum nitride barrier layer does not severely hamper standard material properties. Future work will include refinement of the Sentaurus model to describe charge transport and solve iteratively for piezoelectric/strain coupling.

44

Future characterization will further examine compositional data and dislocation densities through TEM, and actual band effects between nitride layers using electron holography.

POLARIZATION AND PIEZOELECTRIC EQUATIONS

Spontaneous polarization and piezoelectric polarization can be calculated for equilibrium using the following closed form equations from Chen et al.[97] In these equations the strain is calculated from the lattice parameter of the substrate or buffer layer and the layer on top of it. This strain is used to solve for piezoelectric and spontaneous components. Finally, these are used to calculate sheet charge at the interface.

$$\varepsilon = \frac{(a_{sub} - a_{top})}{a_{top}} \tag{3}$$

$$P_{pz}^{AlN} = -1.808 \cdot \varepsilon + 5.624 \cdot \varepsilon^2 \qquad \varepsilon < 0 \tag{4}$$

$$P_{pz}^{AlN} = -1.808 \cdot \varepsilon + 7.888 \cdot \varepsilon^2 \qquad \varepsilon > 0 \tag{5}$$

$$P_{pz}^{GaN} = -0.918 \cdot \varepsilon + 9.541 \cdot \varepsilon^2 \tag{6}$$

$$P_{pz}^{InN} = -1.373 \cdot \varepsilon + 7.559 \cdot \varepsilon^2 \tag{7}$$

$$P_{pz}^{AlxInyGa1-x-yN} = P_{pz}^{AlN} \cdot x + P_{pz}^{InN} \cdot y + P_{pz}^{GaN} \cdot (1-x-y) \tag{8}$$

$$P_{sp}^{InxGa1-xN} = -0.042 \cdot x - 0.034 \cdot (1-x) + 0.038 \cdot x \cdot (1-x) \tag{9}$$

$$\sigma(P_{sp} + P_{pz}) = [P_{sp}(sub) + P_{pz}(sub)] - [P_{sp}(top) + P_{pz}(top)] \tag{10}$$

CHAPTER 5

ALUMINUM NITRIDE BUFFER LAYERS

The improvement of material quality in epitaxially grown layers must start at the wafer level. Barring the use of costly GaN substrates for growth of III-N materials, most materials will be grown on sapphire. The next level of influence over the entire stack's material quality comes from the buffer layer. An ideal buffer layer will transition the vertically grown stack from one crystal structure to another crystal structure, while self-absorbing all the performance degrading dislocations associated with strain energy within itself. In typical nitrides, this buffer layer is GaN on a sapphire wafer.[64], [103]–[106] Though some groups will use a thin low-temperature AlN [107]–[109]. GaN on sapphire buffer technology results in a 30° rotational change from sapphire's pseudo hexagonal crystal structure (rhombohedral) to GaN's true hexagonal structure. However, GaN has commonly been favored due to its lattice parameter that is very near to most developed technological devices: GaN homo devices[110], low In content InGaN [111], and low Al content AlGaN [112].

This chapter will detail the growth and characterization of an aluminum-nitride buffer layer. This AlN buffer layer will be used to produce high quality InN, GaN, and InGaN layers (detailed in subsequent chapters). AlN has two main reasons for being technologically interesting as a buffer layer versus GaN. First, AlN is a slightly closer lattice match to that of sapphire. The other reason why AlN is the ability to "pre-nitride" or "nitridize" the sapphire surface.[113] These two features create an AlN buffer layer with low defect densities.

GROWTH OF ALUMINUM NITRIDE BUFFERS

Layers were grown on sapphire using the aforementioned pre-nitriding process. This process will nitridize the α-Al_2O_3 on the surface and near surface (a few atomic layers). This does a semi-conversion of the surface to AlN, which ultimately makes the epitaxy of the subsequent AlN films better. The pre-nitriding process used was developed by Willimson et al. [114][98], [114] and was held constant throughout the growths. Upon actual buffer layer growth several different growth schemes were tested to discern what if any effect they had on the crystal quality of the buffer layer. These permutations are laid out in Table 5, below.

Table 5
AlN Growth Parameters

Sample	N_2 Flow	Growth Interrupts	MEE smoothing
A	190 SCCM (60 sec) 175 SCCM (120 sec) 160 SCCM (450 sec)	30 seconds between flows	2 iterations
B	160 SCCM (600 sec)	none	none
C	190 SCCM (60 sec) 175 SCCM (120 sec) 160 SCCM (450 sec)	none	2 iterations
D	190 SCCM (60 sec) 175 SCCM (120 sec) 160 SCCM (420 sec)	none	none
E	160 SCCM (60 sec) 160 SCCM (120 sec) 160 SCCM (450 sec	30 seconds between flows	none

Several variabilities in the growth were tested: growth interrupts, modified nitrogen flow, and migration enhanced epitaxy. Growth interrupts were tested to see if with temperature and short time steps defects would self-annihilate in order to lower the crystal's free energy. Modified nitrogen flows were also enacted to try to

promote defect reduction. It is known that when growing III-V compounds with a high V/III ratio smaller grains are nucleated.[115] This occurs due to group-III elements having a surface diffusion length dependent on the flux of the group-V element. Essentially, the group-V element bonds the adsorbed group-III element into the lattice before it can diffuse very far. We hypothesized that by starting with short diffusion lengths a fine network of defects would be initiated at the onset of growth, and as the nitrogen was reduced to near stoichiometry the AlN grains would coalesce producing larger regions of defect free material. Finally, films were tested with and without the effects of migration-enhanced epitaxy (MEE) for the effect of creating smooth surfaces. This was done by supplying several seconds (time=t) of Al followed by t seconds of no beam fluxes, and finally by twice t seconds of N beam.

STRUCTURAL CHARACTERISTICS OF ALUMINUM NITRIDE FILMS

Structural analysis was performed using AFM, RHEED, and XRD. These common characterization techniques were employed to measure surface roughness, average crystal orientation, crystal strain, and defect density. AFM measurements along with RHEED measurements can be seen below. AFM maps in Figure 16 show the effects of the MME surface smoothing step. Figure 16a shows an 8.6 nm absolute change and a 0.647 nm RMS roughness. Figure 16b shows a 5.1 nm absolute change and a 0.640 nm RMS roughness. Interestingly, the MME smoothed map looks visual smoother, yet the statistics for the non-MME smoothed map are better. This is corroborated by the intensity of second and third order reflections in the RHEED image.
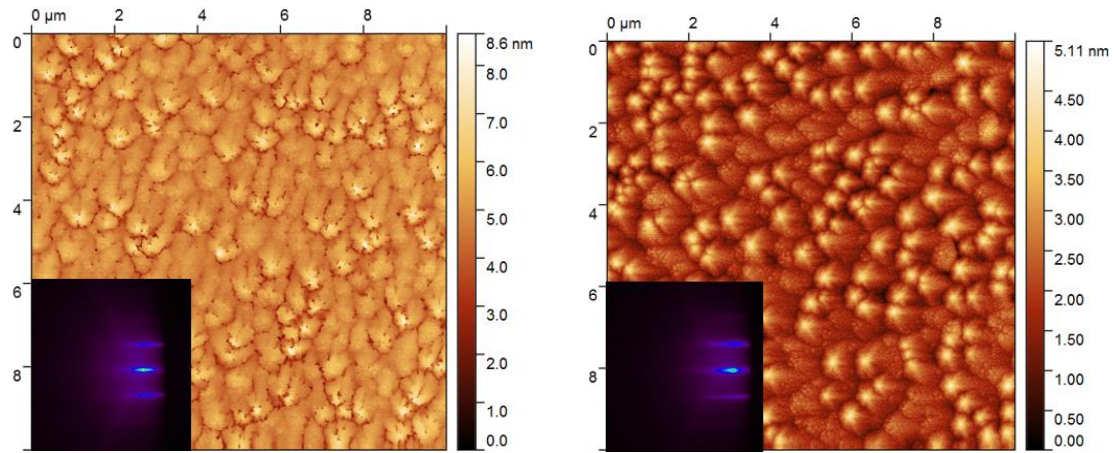
Figure 16. 10 µm x 10 µm AFM measurements with RHEED insets. Figure 16a on the left is with the MME surface smooth and Figure 16b on the right is without the MME surface smoothing.

X-ray diffraction was used to investigate defects, crystal orientation and strain in the AlN sample. XRD data is displayed in Figure 17-Figure 20. The first of these graphs, the double crystal ω-2θ scan of the AlN (0002) peak shows very little strain, as the peaks are not shifted far from their theoretical position. This means that in all samples the films quickly relax nearly all strain associated with heteroepitaxy. Also, it can be seen that the primary peak has strong interference fringes around it. These Pendellosung fringes are indicative of material with a high degree of vertical coherence in the crystal structure, as they are created from the interference of diffraction at the top and bottom of the sample. Furthermore, the spacing can be used to calculate the average thickness for the films, in this case thickness is 157 nm, nearly on spot with the 160 nm target. The discrepancy is likely due to poor diffraction from the highly defective several nanometers of material right at the interface with sapphire.

49
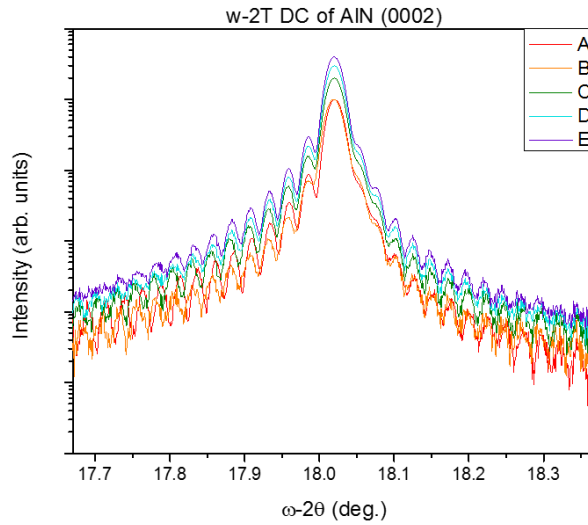
Figure 17. ω-2θ scan of the AlN (0002) diffraction peak accompanied by strong interference fringes.
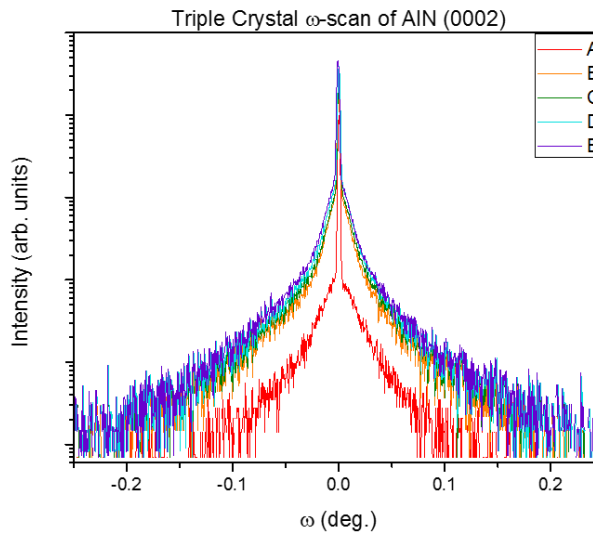
Figure 18. ω-scans of the AlN (0002) diffraction peak. All samples show a weak broad diffuse scatter peak and a strong central coherent peak.

The next up in the suite of XRD scans are the TC ω-scans. These give information about how well aligned are the basal planes of the AlN, as well as can be used to estimate dislocation densities. The strong central peak and broad-base are classic of a film[116]–[118] with a very high degree of crystallite alignment and a moderate TDD (~10^7 /cm^2). By deconvoluting the two peaks, a FWHM can be extracted

50

for the broad diffuse peak under the strong coherent peak. In this case, the FWHM of the underlying peaks is in the neighborhood of ~100 arc sec. Using Ayers[101] empirical formula for TDD estimation from rocking curves, it can be approximated that these films have dislocations (with burgers vector components in the c-plane) on the order of magnitude 10^7 /cm^2 as was previously mentioned.

Finally, reciprocal space maps of the symmetric 0002 peak and the asymmetric 10-15 peak are given. The shape of these maps give more insight to nature of the defects in the material. The (0002) map shows by its cross-like nature that defects are confined to running perpendicularly in the film. The tail on the down-side is the map representation of the interference fringe from the ω-2θ scan. These conjectures are verified by the horizontal ellipsoid nature of the 10-15 map. Defects running in any skew direction will tend to smear the pattern from its horizontal norm.
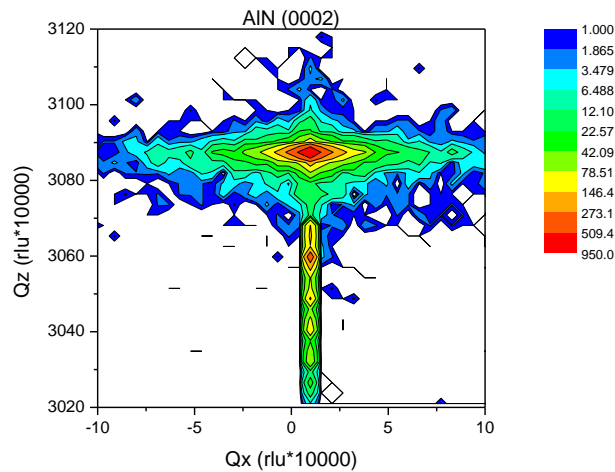
Figure 19. RSM of the 0002 diffraction condition.
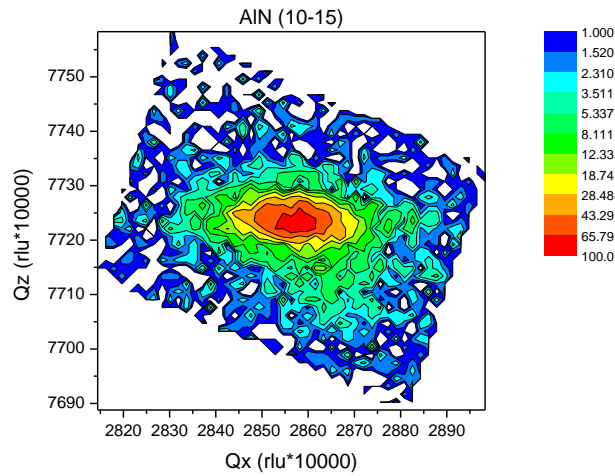
Figure 20. RSM of the asymmetric (10-15) AlN diffraction peak.

CHAPTER CONCLUSION

Growth of a multitude of different films representing different permutations of growth efforts to reduce defect density and increase crystal quality. AlN, by XRD shows very low density of threading defects 10^7 /cm^2. However, the individual efforts of growth permutations show very little difference in the crystal quality (by XRD) and as static growths are the simplest, these are recommneded. However, from the AFM section it is interesting to note that the migration enhanced epitaxy appears to smooth the surface of the crystal yet the actually RMS roughness is relatively unchanged.

This material is significantly less defective than the buffer–layer in the previous chapter and creates a <1 nm RMS surface roughness. Subsequent chapters will build upon this technology.

CHAPTER 6

INDIUM NITRIDE FOR HOT CARRIER SOLAR CELLS

The single greatest challenge with classic photovoltaic devices is that both their absorption (and therefore current) as well as their voltage is governed predominantly by their band gap. In order to increase one, the other must decrease. It has been theorized that a device known as a hot carrier solar cell could be a solution to this problematic paradigm.[119]

A hot carrier solar cell is a device in which electrons can be extracted at energies above the conduction band edge and holes below the valence band edge. In theory this would allow a low band gap material with normally high absorption to also have a higher than normal voltage. This type of device has been predicted to have a theoretical efficiency of 66%.[119]

Three features are required to make an effective hot carrier solar cell: a selective energy contact, low band gap absorber material, and a mechanism for prolonging excited carrier populations. A selective energy contact is a method for extracting carriers at a specific energy level. This would ensure that the voltage obtained from the device would be as a function of the elevated carrier energy and not the band gap energy. The most feasible device for such a contact would be a resonant tunneling diode(Figure 21), which has demonstrated good current densities.[120] Such a device could be constructed from a barrier-well-barrier stack of AlN, GaN, AlGaN, or InGaN.
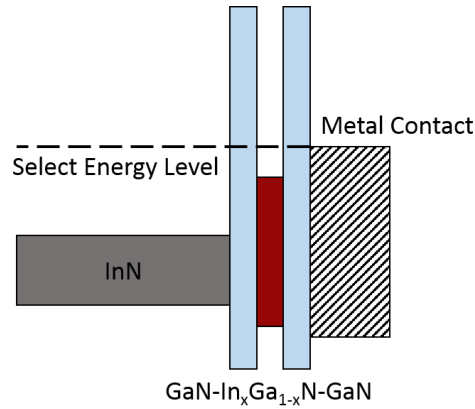
Figure 21. An example of a conceptual RTD as an energy selective contact.

The final and perhaps most crucial requirement for a hot carrier solar cell is a mechanism to prolong the lifetime of carriers at an excited state above the band edge. One phenomenon that has gained some attention as a possible method is the phonon-bottleneck effect.[121] The phonon-bottleneck effect may be realized when there is a large phonon band gap in the material, and therefore the decay from optical phonons to acoustic phonons is suppressed. Thus, if an electron relaxes through generation of optical phonons there is a probability that the optical phonon can excite another electron maintaining a steady state of "hot electrons." Large phonon band gaps appear in materials where the atomic masses of the cation and anion are dissimilar. The more dissimilar the masses, the better that ability for a phonon bottleneck.[121]

The requirements of a low optical band gap and large phonon gap set strict requirements for materials selections. InN is potentially the best material to meet both of these requirements. The optical band gap of InN is 0.65 eV at room temperature[13], [14] and it has a wide phonon gap.[121] This mean that InN is positioned to absorb 88% of the photon current in an AM1.5G spectrum, by contrast

silicon can only absorb 62%. If excited electrons and holes can produce a voltage in excess of the band gap then a hot carrier device may be realized.

CHALLENGES OF GROWTH AND SAMPLE SYNTHESIS

The application of InN for an absorber and "hot carrier reservoir" in a hot carrier device requires material of high crystal quality at thicknesses that are optically opaque. This requirement is challenging when growing heteroepitaxial layers on lattice mismatched sapphire wafers. This lattice mismatch causes dislocations in the crystal structure that may ultimately diminish electrical properties.

By focusing on material growth conditions, better quality InN can be achieved. The common technique for achieving high quality films on lattice-mismatched substrates is to grow a buffer layer that will accommodate strain energy and the subsequent crystal defects. It has been shown that AlN on sapphire demonstrates an extremely low degree of crystal tilt and a low concentration of threading dislocations.[116], [118] These properties of AlN make it an interesting candidate as a buffer layer for InN films grown on sapphire.

Films were grown on wafers of c-plane sapphire. Wafers were degassed at 900 °C for 20 minutes, and nitridized at 350 °C for 20 minutes. A 5-minute AlN buffer layer, similar to the work of the previous chapter, was grown at 800 °C. Then a 25-minute InN film was grown at 400 °C.

Working under the hypothesis that increased N flux during nucleation decreases crystal size laterally, which would provide strain relief from lattice mismatch, films were initiated under N rich fluxes (~ 25% excess N_2 flow). After film

initiation, nitrogen was reduced to near stoichiometry erring on the side of nitrogen rich. Near stoichiometric conditions are established based on the response of the nitrogen RGA signal when shuttering group III sources.

INN MATERIAL STRUCTURAL QUALITY

Cross-sectional transmission electron micrographs with sensitivity to screw and edge dislocations can be seen in Figure 22. These images depict a sharp interface between the AlN buffer layer and the InN film. The surface of the InN film is rather rough, possibly due to a quasi-2D growth mode and the chemical treatment of the dislocation trenches during TEM sample preparation. The two imaging conditions highlight the different types of defects present in the material. Both AlN and InN films depict a low number of screw type dislocations (Figure 22a). The density of edge dislocations is at least an order of magnitude higher in AlN layer than in InN layer (Figure 22b). The $[11\bar{2}0]$ micrograph (Figure 22b) also demonstrates the columnar nature of AlN and InN films. Both micrographs demonstrate appearance of closed dislocation loops at the bottom of the InN layer, created above the AlN-InN interface at the final stage of the defect creation process.[122] The density of these loops at the bottom of AlN layer is lower but also visible. The film thickness from these images is 117 nm for AlN and 350 nm for InN layer.
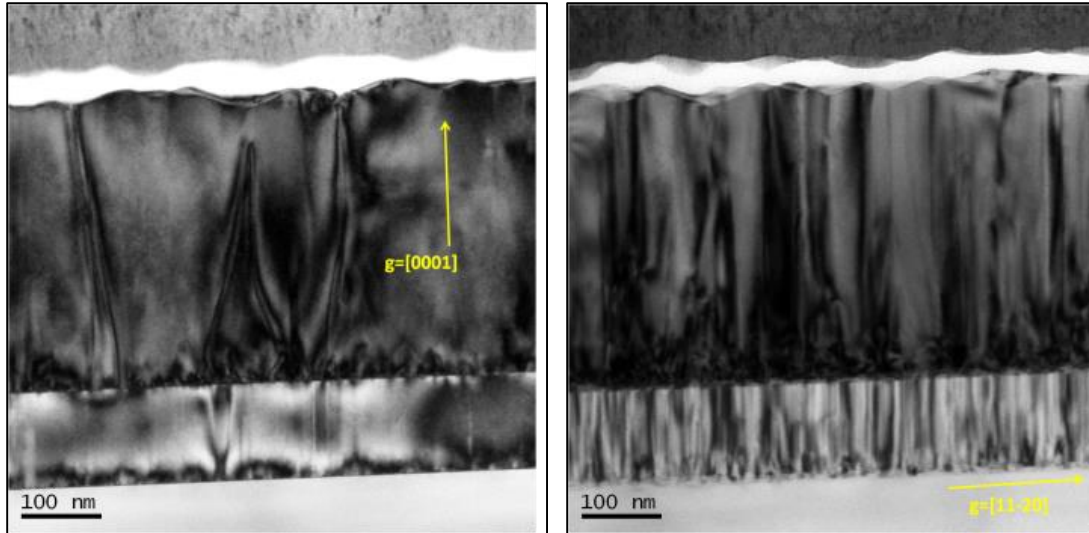
Figure 22. These micrographs depict the different dislocations based on diffraction condition. The image on the left, Figure 22a, (g=[0001]) highlights screw dislocations. The image on the right, Figure 22b, (g=[11$\bar{2}$0]) highlights edge dislocations. Both images visualize closed dislocation loops at the bottom of the layers.

The double-crystal wide-angle ω-2θ scan in Figure 23 shows an extended interference pattern around AlN(0002) peak and an additional strain in each of the epitaxial layers: 1% tensile in InN and 5% compressive in AlN. Triple-crystal ω-2θ scans for each of these peaks (Figure 24) demonstrate interference fringes around the main layer peak. Being a sign of high vertical coherence of the scattering layer due to the low density of edge segments of closed dislocation loops in the volume of the layers, interference fringes allow estimation of film thicknesses.[123] The AlN layer is 108 nm thick, while InN is 340 nm thick, in good agreement with TEM data.

The noticeable asymmetry of ω-2θ rocking curves is related to a small elastically stressed sub-layer at the bottom of the layers. Compressive stress was induced by ramified closed dislocation loops, created here (Figure 22) at the final stage of the elastic stress relaxation. [122], [123]

X-ray triple-crystal ω rocking curves, collected at AlN and InN peaks, can be seen in Figure 25. Both curves show a specific shape with a strong and narrow

57

coherent central peak and a broad diffuse peak.[117], [124], [125] The FWHM of the central peak (7.2 – 8.4 arcsec) reveals extremely low ω tilt between adjacent crystal domains. The lateral coherence of epitaxial layers, corresponding to this FWHM is ~ 6.4 – 7.4 µm. FWHM of the diffuse peak allows estimation of the number of closed dislocation loops located at the bottom of the layer.[117], [126] Based on this the approximate values for the density of dislocation loops is 2×10^8 /cm² and 3×10^7 /cm² for the InN and AlN layers, respectively. Asymmetrical RSMs (not shown here) revealed significant twisting of crystal domains around the growth (φ) axis (especially in the AlN layer), caused by edge dislocations, surrounding crystal domains.[116], [127]
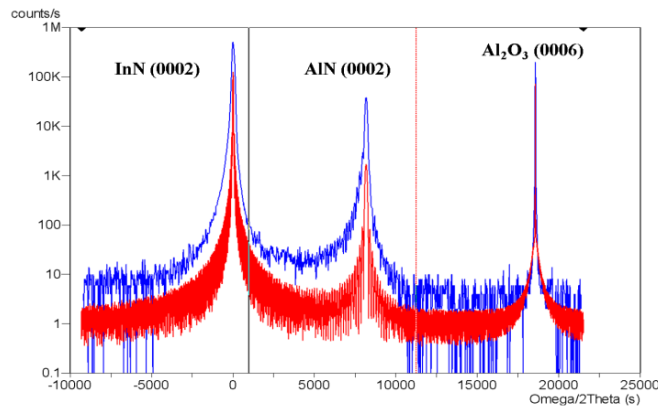
Figure 23. ω-2θ scans. The blue scan is experimental and the red scan is simulated. The subtle shifts in peak position correspond to compressive and tensile strain in AlN and InN, respectively.
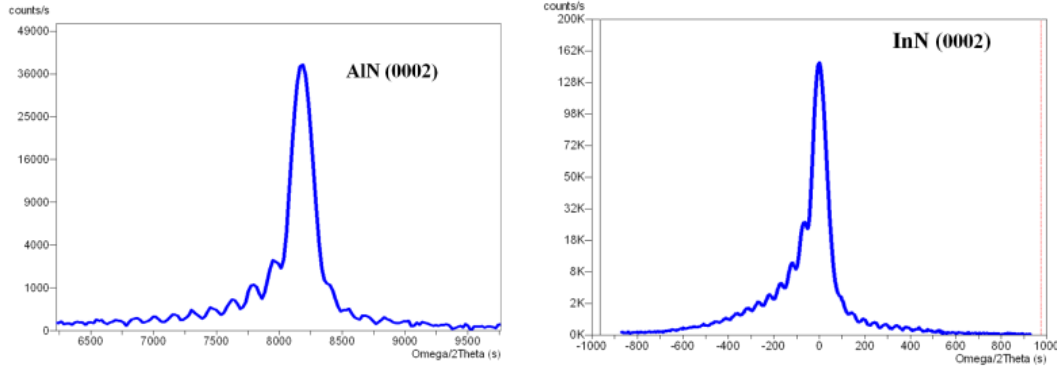
Figure 24. High-resolution (triple crystal) ω-2θ scan of the (0002) peaks from both the AlN buffer layer and the InN film. The presence of interference fringes signifies a low density of edge segments of dislocation loops in the volume of the layer. Asymmetry is related to additional elastic stress at the bottom of the layers.

These structural features reveal highly crystalline epitaxial layers with negligibly tilted small (in lateral directions) crystal domains. X-ray diffraction on such layers has to lead to extended strong interference pattern on ω-2θ RCs and a very narrow central coherent peak on ω RCs, typical for single-crystal epitaxial layers with high spatial coherence.[117], [118], [122], [123] Such coherent scattering is possible, because in contrast to 60° dislocation loops and their dislocation trenches in cubic compounds, vertically propagated edge and screw dislocations in hexagonal layers do not deteriorate spatial coherence of epitaxial layers, while diffused radiation, scattered by closed dislocation loops at the bottom of the layers (Figure 22), is insufficient to noticeably suppress coherent scattering.[122], [123], [125], [126]

Peculiar to single crystal layers, it has been shown that textured layers of small crystalline domains with almost no in-plane (φ) misorientation, do not have suppressed 2D growth mode.[127] X-ray clarified that under growth conditions edge dislocations complete reconstruction of the growth surface and create crystal domains, but do not deteriorate atomic surface migration and 2D growth mode.[123]

59

Under ideal growth conditions, long delays between creation of edge dislocations and formation of closed dislocation loops at the bottom of the layers, typical for III-N epitaxial layers [122], [123], allows growth of rather thick fully relaxed epitaxial layers with high spatial coherence.[116], [118], [122], [123], [125] Still, crystalline defects created during relaxation of elastic stress can significantly deteriorate other physical properties of grown epitaxial layers: photoluminescence (PL), carrier mobility, phonon scattering, etc.
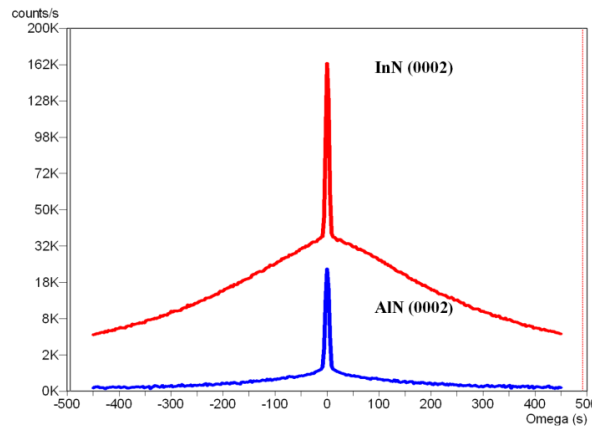
Figure 25. Triple crystal ω scans of both the AlN buffer and the InN film. The intensity difference is largely due to amount of material diffracting. The FWHM of the central peak is about 7-8.4 arc sec in both cases. The InN diffuse FWHM is ~460 arcsec, while the AlN FWHM is ~180 arcsec.

Preliminary Raman spectroscopy indicated an E2 (high) peak with a FWHM of 4.2 cm^{-1}. Compared to a 5.5 µm thick (15.5 times thicker) reference sample (FWHM of 3.0 cm^{-1}), there is a peak shift of ~1.5 cm^{-1}, indicating noticeable secondary elastic stress in the sample film. The low temperature (78 K) PL peaked at 0.672 eV, FWHM is ~0.04 eV nearly the same as the reference structure, while the intensity is about 16 times lower. Hall mobility is 646 cm^2/V-s, 3 times lower, while electron concentration is ~3 x 10^{18} cm^{-3}, 9 times higher, in comparison with the reference sample.

Which crystalline defects are mostly responsible for deterioration of physical properties of InN epitaxial layers is the main subject for further investigations. Meanwhile, the main growth efforts will be concentrated on the improvement of growth conditions to amend physical properties of epitaxial layers.

CHAPTER CONCLUSION

Films of InN were researched at a preliminary level for use in hot carrier solar cells. The primary focus being on increasing crystal quality when grown on lattice mismatched sapphire. An AlN buffer was used to accommodate the initial elastic strain between a sapphire (0001) substrate and an InN epitaxial layer to improve crystal quality of the InN.

Film thicknesses determined by XRD interference fringes and cross-sectional TEM measurement average 113 nm for AlN and 345 nm for InN. Based on growth conditions, these films were grown at 22.6 nm/min and 13.8 nm/min for AlN and InN, respectively.

Both AlN and InN epitaxial films exhibit, by TEM and XRD, a columnar textured domain structure with a low density of threading dislocations and a low degree of domain tilt around the horizontal (ω) axis. The columnar nature of the crystal domains is a characteristic sign of nitrogen polar materials.[16] Discrepancies with literature of growth temperatures for n-polar and those reported here are likely due to offsets stemming from differences in growth reactor setup and the unusual nitrogen source. Nevertheless, these methods have produced films that can accommodate elastic strain almost solely by edge dislocations. Leading to films of InN

61

grown on sapphire via an AlN with crystal misorientation being practically only around the vertical (φ) axis.

CHAPTER 7

HIGH GROWTH RATE GALLIUM NITRIDE

MBE has unique advantages over MOVPE due to its inherent lower background contamination, ability to make abrupt stops of incoming growth species (important for sharp quantum wells), and kinetically driven capability to access metastable phases that are not available to growth processes of thermodynamic equilibrium, as has been demonstrated in previous chapters. However, any commercial interest in MBE has been passed over due to slow growth rates that make it hard to meet demand in this challenging industry. These slow growth rates are mostly due to the low fluxes of active nitrogen associated with conventional plasma nitrogen sources. [128], [129] The ENABLE technique described in Chapter 2 and demonstrated throughout this thesis is ideally capable to overcome this long time drawback of MBE.

ENABLE is capable of delivering high flux of neutral nitrogen atoms (or other gases as well) as the active species to the surface of a wafer.[130] This technique has the potential to keep pace with the Ga fluxes supplied by the industry standard Ga effusion cells. This should lead to higher growth speeds for gallium nitride films by MBE. These high speed growth rates and their effects on structural and luminescent properties will be explored herein.

EXPERIMENTAL

Film growths were performed at a background pressure of 3.1×10^{-9} Torr during the time prior to sample growth. Samples were rotated during growth at 5 rpm to promote film uniformity. Transients of each signal are used to determine deviations

from stoichiometry. A gallium beam is supplied to the sample surface of the sample from a Veeco SUMO thermal evaporator. This provides high quality Ga flux uniformity across the wafer surface.[70] The ENABLE source was used to supply the nitrogen beam.

Samples were grown on two inches c-plane oriented α-Al₂O₃ wafers. Wafers were outgassed for 30 minutes at 900 ºC followed by nitridation at 350 ºC for 30 minutes. An aluminum nitride buffer layer, based on the work detailed in Chapter 5, was grown at 850 ºC for 10 minutes at a nominal growth rate of 15 nm/min. Subsequently, the GaN layer was grown for 10 minutes at 850 ºC with varying growth rates. Growth rates were based on a nominal growth of 15nm/min for a Ga cell base temperature of 950 ºC. Samples were also grown with the Ga cell base temperature at 1000 and 1050 ºC. Under the assumption that the ratio of vapor pressures (based on Equation (11), where T is in Kelvin and P is in atmospheres [131]) at these temperatures will produce an equivalent ratio in Ga flux to the sample surface it was estimated that the growth rates should be 30 nm/min and 60 nm/min, respectively. Growths were not investigated at higher speeds due to concerns of the Ga cell spitting above 1050 ºC. However, it should be noted that the ENABLE source was only running at 20% nitrogen capacity for the fastest growth. In keeping consistency with other growth protocol on this tool (focused on In-rich InGaN [98]) films were grown in a slightly nitrogen rich regime. This was verified by monitoring the transient of the nitrogen signal in the RGA after metal shuttering.

$$\ln\left(P_{Ga,vap}\right) = \frac{-14,900}{T} - 0.515 \cdot \ln(T) + 7.34 \tag{11}$$

The thickness and surface roughness of the samples were measured using a Woollam variable angle spectroscopic ellipsometer. Incident light with wavelengths ranging from 400 to 800 nm was used. The resulting data was fitted to n (index of refraction) and k (extinction coefficient) values for GaN and AlN. Surface roughness at the AlN-GaN interface was assumed to be negligible. This was based on the RHEED pattern of the AlN layer showing strong surface reconstruction, indicative of a near atomically flat surface.

Structural properties of the samples were characterized using a PANalytical MRD high resolution X-ray diffractometer (HRXRD). A hybrid X-ray mirror with asymmetrical Ge (220) 4-bounce crystal produces an incident Cu-K$_{\alpha 1}$ X-ray beam with λ=0.1540598 nm and 19 arcsec divergence. A triple crystal scheme (TC) utilizing a three-bounce Ge(220) analyzer crystal in front of the detector was used to collect high resolution ω-2θ and ω scans to separate coherent and diffused scattered radiation. A double crystal scheme (DC) with only a receiving slit on the detector was used to perform rough alignments and collect ω-2θ and ω-scans. A JEOL JSM 6300 scanning electron microscope (SEM) equipped with MonoCL2 cathodoluminescence spectrometer was used to measure the optical properties of the samples.

RESULTS AND INTERPRETATIONS

Ellipsometry values for roughness and thickness are presented in Table 6. Most of these values track well with the X-ray diffraction based calculations. Both of the measured values trail the vapor pressure curve approximations. The offset in growth rates is due to the slight inaccuracy of the known growth rate. The reference

growth rate was thought to be 15 nm/min, but these conditions yielded a growth rate of 13 nm/min.

Table 6

X-Ray Diffraction and Ellipsometry Measurements

		X-Ray Diffraction					Ellipsometry	
		2θ Pos.	Coh. FWHM	Diff. FWHM	DC FWHM	Thickness[1]	Thickness[2]	Roughness
"15	AlN	35.92º	0.0022º	0.0353º	0.0290º	160 nm	177 nm	--
nm/min"	GaN	34.41º	0.0025º	0.0470º	0.0396º	132 nm	134 nm	3.0 nm
"30	AlN	35.98º	0.0029º	0.0333º	0.0360º	154 nm	163 nm	--
nm/min"	GaN	34.50º	0.0029º	0.0602º	0.0510º	275 nm	283 nm	4.5 nm
"60	AlN	35.96º	0.0036º	0.0334º	0.0350º	160 nm	181 nm	--
nm/min"	GaN	34.57º	0.0034º	0.0343º	0.0280º	--	782 nm*	15.3 nm

In Table 6, shown above, the "Coh. FWHM" column represents the full-width-half-maximum (FWHM) of a Gaussian peak representative of the narrow coherent peak for the TC ω-scans. The "Diff. FWHM" represents the FWHM of the complimentary broad diffuse peak from the same de-convolution process of TC ω-scan. The "DC FWHM" values are taken from ω-scans with double crystal scheme and no receiving slits. Thicknesses 1 and 2 are from XRD and ellipsometry, respectively. The thickness for the "60 nm/min" speed GaN does not follow the trend of the other two that is falling just short of the vapor pressure approximation. This value produced a high mean-squared error and is likely off due to surface roughness and non-ideal n & k values.

A symmetric ω-2θ scan of all three samples is shown in Figure 26. The GaN (0002) and AlN (0002) can be clearly seen, with no irregular phases present. Additional scans (not shown here) included the Al_2O_3 (0006) substrate peak. These

scans confirmed that measurements were made with the sapphire peak well aligned in the diffractometer at 2θ=41.67°.
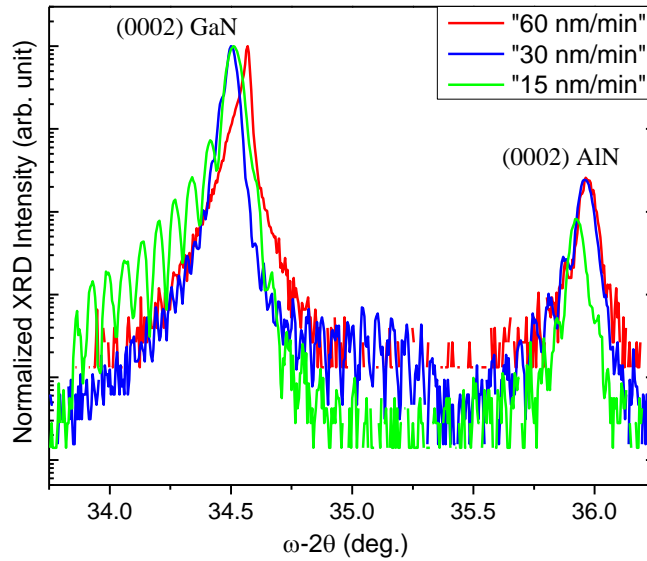
Figure 26. A semi-log plot of ω-2θ scans performed in TC mode about the GaN and AlN (0002) peaks.

The high resolution TC ω-2θ scan resolves interference fringes (i.e. Pendellosüng fringes) about the main diffraction peaks. The angle spacing of the fringes can be used to estimate the layer thickness.[132] The fringes around the AlN peak correspond to a thickness of ~160 nm for all three films, and hence a growth rate of 16nm/min. The GaN peaks for the "15 nm/min" and "30 nm/min" both have fringes, while the "60nm/min" does not due to higher volumetric structural deteriorations. The interference fringes on the former two correspond to thicknesses of 132 and 275 nm, respectively. These values come from growth rates of 13.2 and 27.5 nm/min for the nominal "15nm/min" and "30nm/min" respectively. This is in close agreement with the initial vapor curve based approximations, and nearly identical agreement with the ellipsometry data. If it were to be assumed that the "60nm/min" sample follows the

67

same trend it would have a thickness of 550 nm and a growth rate of 55 nm/min. It is a noteworthy trend the Pendellosüng fringes become more diffuse with faster growth rates. This is likely due to increased bulk defect densities with increased growth rates, defects which may not show up in ω-scans.
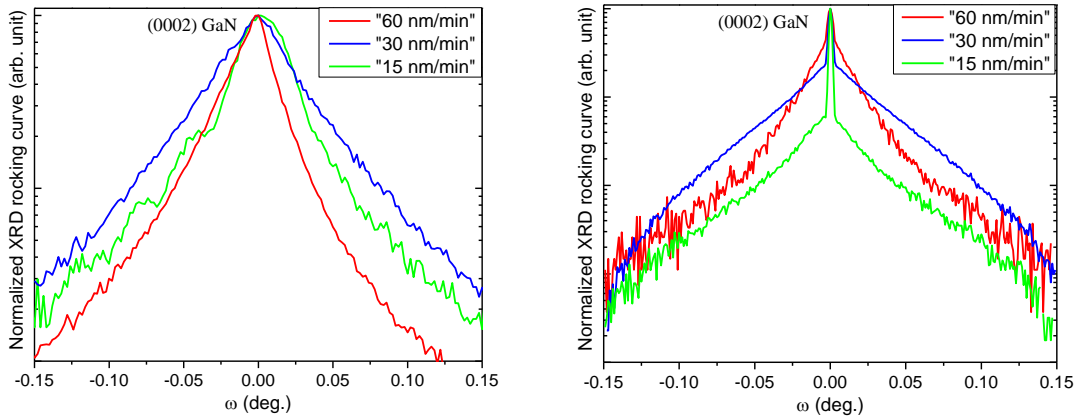
Figure 27. The graph on the left, Figure 27a, is of the GaN (0002) peak in double crystal mode. The graph on the right, Figure 27b, is of the same peak measured in TC mode.

Figure 27a, the ω-scan with the double crystal schematic was collected with no receiving slits. Figure 27b, the triple crystal schematic, uses the analyzer crystal to separate coherent diffraction of the lattice planes from diffuse radiation due to crystal imperfections. These scans have been de-convoluted into two Gaussian peaks representing the coherent and diffuse components. The FWHM for each of these component peaks is listed in Table 6. For the double crystal and diffuse scattered radiations the FWHM is never wider than 0.083º or 300 arcsec. This value been classically assigned as benchmark device grade GaN. There have been accounts that narrower peaks can lead to material with worse device quality.[23] Additional characterization of background carrier concentrations, TEM, and polarity measurements would indicate if this is valid for these samples.

Cathodoluminescence (CL) spectra of the three samples, taken at 295 K, are shown in Figure 28. The "60 nm/min" sample exhibits a near-band-edge emission (NBE) at 364 nm with a FWHM of 11 nm. Two additional broad emissions are observed at ~ 450 (blue) and 575 nm (yellow). The origin of the latter band is associated to nitrogen vacancies.[133] As the growth speed decreases, the intensity of the NBE and of the yellow band quench. A

Figure 28. Cathodoluminescence of the different samples.

decrease in the yellow band luminescence may be associated to a decrease in the nitrogen vacancy density (i.e. material grows more stoichiometrically). CL images taken at the NBE emission of the three samples are shown in Figure 28. We observe an improvement in the film surface quality from large grains (~500 nm) to smooth surfaces as the growth speed decreases. For example, "30 nm/min" exhibits bright and dark regions. The dark regions correspond to regions with lower NBE intensity, possibly due to lower crystalline quality. The decrease in the NBE for the lowest growth speed sample may be explained by a lower background carrier concentration.

CHAPTER CONCLUSION

The use of the ENABLE technology has been implemented to deliver high fluxes of active nitrogen for growth of gallium nitride. These high fluxes have been used to investigate nominal growth rates of 15, 30, and 60 nm/min. Structures all show narrow FWHM for ω-scans of (0002) GaN and interference fringes on the AlN buffer layer. The nominal 15 and 30 nm/min films show interference fringes around the ω-2θ GaN (0002) peak, indicating high vertical coherence of these films. The 60 nm/min film shows no interference fringes and broader almost diffuse ω-scans, indicating that at high growth speeds the crystal quality is more deteriorated. This trend is also seen in the ellipsometry fittings. Both the ellipsometry fittings and the interference fringe spacing give good agreement for thicknesses in the "15 nm/min" and "30 nm/min" sample thicknesses. Real rates were slight slower than anticipated, 13 and 28 nm/min. However, the relative ratio for the rates was as expected.

All samples show band edge or near band edge emission in the cathodoluminescence measurements. This indicates that the growth rates can be pushed to high speeds while still sustaining crystal quality good enough for photo-active material. Some broad low intensity emissions in the blue and yellow range start to show up for the 60 nm/min GaN, likely due to deviations in stoichiometry.

The characteristics of stable growth rate, narrow rocking curves, and photoactive material are all promising results. They indicate that using ENABLE as a source of active nitrogen species, nitride MBE can achieve growth respectable material at growth rates up to at least 55 nm/min. This rate of 3.3 µm/hr was achieved with the ENABLE source at 20% of maximum nitrogen capacity opening the possibility for MBE to achieve even faster nitride based growth.

CHAPTER 8

A WIDE BAND GAP REFRACTORY INDIUM-GALLIUM-NITRIDE SOLAR CELL

The III-N material class has demonstrated unique properties that are of significant interest for photovoltaic applications. The final property III-N property to be discussed in this thesis is temperature stability. This shall be examined through the efforts of attempting to build an InGaN photovoltaic device which can operate at elevated temperatures. It shall be briefly described the ways in which high temperature operation can actually improve device performance for the nitrides (unlike nearly all other semiconductors) followed by the type of application(s) that can benefit from such a device. Then the cell design shall be discussed followed by the fabrication. Finally, significant emphasis will be placed on the electrical performance of the resulting device(s).

The III-N materials have a proven track record in high temperature applications[110], [134], [135] and have been lightly investigated as candidates for photovoltaics operating at elevated temperatures [136]–[140]. This refractory nature occurs through chemical stability and their inherent wide-band gap nature. GaN and InGaN are known for having good chemical stability even at elevated temperatures[23] and possess a high dissociation temperature[27] as was previously mentioned. As a result of the wide-band gap nature of GaN and low In concentration InGaN, these semiconductor materials retain their semiconducting properties at temperatures much greater than most semiconductors. The largest factor to contribute to this is thermal excitation of intrinsic carriers (n_i) which have a direct effect on J_0, the dark current.

Design and construction of efficient InGaN solar cells has historically been limited by material quality (as has been previously discussed). This limitation revolves around needing high In content material for a solar relevant band gap, yet these In % alloys are highly defective. In this project, due to temperature based band gap narrowing InGaN compositions are red-shifted further into the solar relevant ranges while still keeping the In fraction low and thus material quality higher. Figure 29 shows the change in InGaN band gap with both temperature and In composition. An additional benefit while constructing a III-N device to be operated at elevated temperature is dopant ionization. The temperature will ionize a greater fraction of the historically difficult to ionize magnesium dopants in the material.
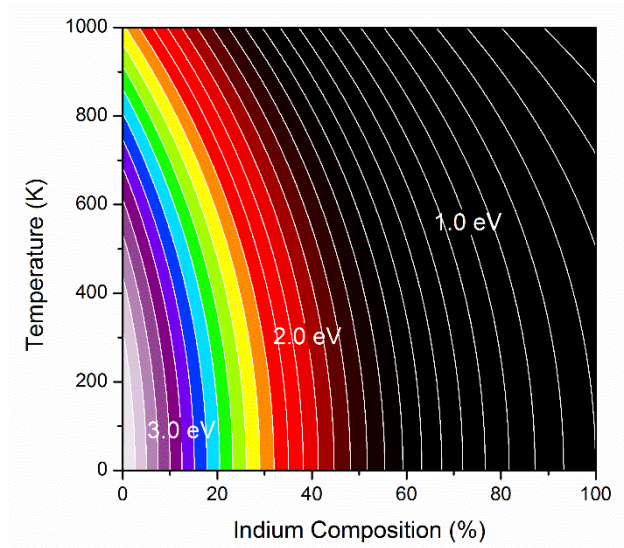
Figure 29. Contour plot of InGaN band gaps against temperature and indium. Band gaps are color coded to match the visible spectrum. Calculated using Equations (1) & (2) and values from

Table 1.

High-temperature photovoltaic devices have niche applications in hybridized solar plants and inner solar system space probes. The latter of these two applications is very niche but still relevant for research purposes with limited but definitive

interest from space exploration for solar cells that can operate at >400 °C. The former application seeks to combine the best of both concentrated solar power and concentrated photovoltaic power. This is to achieve a low $/W cost of electricity in real time (CPV) and a method for energy storage (CSP) thus providing "solar power" after the sun has set.[141] This application has prompted the design of the cell contained herein.

DESIGN, GROWTH, AND FABRICATION OF AN INGAN BASED SOLAR CELL

The application of an InGaN solar cell in a concentrated solar thermal plant appears to require an integrated analysis of energy conversion by both photovoltaic and conventional Rankine cycle mechanisms. However, in practicality there is a fair amount of leeway in design criteria owing to aspects of the working-fluid flow rate, the thermal storage capacity, and the thermal receiver's ability to be a broad band absorber. Furthermore, the cell will be thermally synced with the thermal receiver, and thus all inefficiencies (which become heat) in the cell will be able to be absorbed by the thermal receiver. This means the cell design should be optimized to create the most amount of electricity possible for the InGaN technology, and the balance of the solar spectrum (and device inefficiency) can be captured by the thermal receiver. The overarching goal for this project was to create a two junction InGaN tandem capable of converting the UV and visible sections of the solar spectrum with loose targets on bandgap to accommodate for challenging material quality. It was predicted that rough targets should be $E_G \approx 2.7$ eV for the top cell and $E_G \approx 2.0$ for the bottom cell. At this point it is pertinent to introduce additional nomenclature for referring to the band gap at a given temperature, $E_{G,Temp}$, since both temperature and In % can change the band

gap. The remainder of this chapter shall focus on the top cell for the very simple reason that the author worked exclusively on the top cell.

All iterations of the top cell were grown using MOVPE. Precursor gases consisted of trimethylgallium, trimethylindium, bis(cyclopentadienyl)magnesium, silane, and ammonia. Growths were performed on patterned sapphire substrates with a thick >2 μm UID-GaN buffer layers for threading dislocation reduction. This is followed by a thick GaN(Si) n-type base with moderate doping throughout and strong doping near the top. Next the MQW stack, which is the active absorber region for the cell, is grown, and it consists of InGaN wells and GaN barriers with varying widths and doping levels depending on the growth run. The order of magnitude for thickness in this region is 50 nm to 200 nm. Finally, a 150 nm GaN(Mg) p-layer is grown. This region has high concentrations of magnesium, $1x10^8$ /cm^3, since Mg has such low carrier activation percentages. Cells where grown and tested with bulk (20-100 nm) InGaN absorber material, however these yielded very poor voltages due to compromised material quality and thus were ruled out as viable options (and not reported here).

Fabrication of devices from wafers with growths was performed using a series of photolithography, etching, and deposition steps. Unlike normal silicon photovoltaic cells, these more advanced fabrication techniques are needed to create mesa structured cells. Mesa structures are necessary to make electrical connection to the n-region of the solar cell since the sapphire wafer is insulating. The growth and fabrication results in devices similar to what is seen in Figure 30. Contact metals for for n-GaN are Ti/Al/Ni/Au and for p-GaN are Ti/Au/Pt. A layer of ITO is used between the p-GaN and the Ti/Au/Pt contacts to assist with lateral mobility.
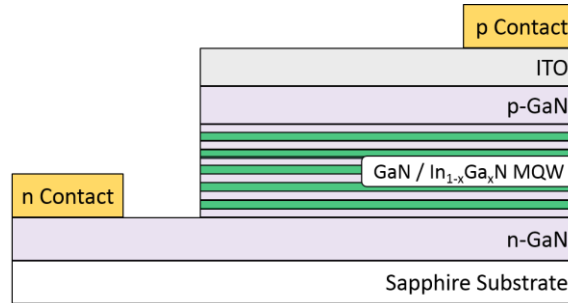
Figure 30. Generic schematic of the top cell structure. Number of quantum well-barrier periods and all layer thicknesses are variable run-to-run.

ELECTRICAL MEASUREMENTS OF THE INGAN CELL

Electrical measurements of InGaN solar cells are useful to learn about how the device behaves under different conditions. By correlating its performance in different tests with known growth parameters, cells can be iteratively redesigned to make the best device possible. Electrical tests were carried and will be showcased herein: external quantum efficiency (EQE), and I-V measurements both in dark and under illumination. These tests give information on parasitic absorption, effects of sheet resistance, shunt resistance and ultimately the cell's efficiency. When technologically and logistically feasible these electrical measurement tools were augmented with a temperature stage. This enabled routinely carrying out tests from room temperature to 450 °C and in some cases up to 600 °C.

External quantum efficiency measures a device's ability to convert light to electricity as a function of wavelength. Typically, these measurements are performed at short circuit, though voltage bias can be applied. EQE measurements of the top cell show that very little current is actually extracted from wavelengths shorter than the GaN absorption edge. This could be due to surface reflection, free-carrier absorption in the ITO, or short minority carrier lifetime's in the GaN. The majority of the EQE

signal comes from absorption in the InGaN quantum wells, fine features will be discussed later. An over-arching trend in all samples is a relatively low (less than 80% peak) EQE in the target region, 365 nm to 450 nm. This low EQE is attributed to incomplete absorption of the available light due to an inadequate effective thickness of InGaN across the MQW. On the tail of the curve, "red-response", it is possible to discern information about effects at the back of the cell. The inflection point in the red-response can be used as one form of measuring the effective band-gap of the cell. Finally, when applying these wavelength dependent conversion efficiencies to the wavelength dependent photon flux of the solar spectrum it is possible to determine the J_{SC} of the cell.

$$J_{SC} = \int_{280\text{ nm}}^{4000\text{ nm}} EQE(\lambda) \cdot J_{solar}(\lambda) \cdot d\lambda \tag{12}$$

EQE measurements versus temperature are informative of several aspects of cell performance. Firstly, it shows band-edge shifts as a function of temperature. This can be seen in the blue response where the low QE p-GaN gives way to the main InGaN absorber, as well as the devices effective band gap from the red-response. Additionally, it is theorized that higher temperatures will increase carrier escape from the quantum wells, thus increasing the EQE from the absorber region.[137] J_{SC} will be representative of the current from the entire device (such as measured by I-V) and will be a convolution of increased EQE from the MQW as well as the device absorption red-shifting to absorb more of the solar spectrum. EQE is pivotal in deconvoluting these effects. Finally, this knowledge can be taken one step further by augmenting the data with transmittance and reflectance data to generate a curve known as internal quantum efficiency, see Equation (13). This IQE curve shows the wavelength

76

dependent efficiency of extracting an electron from the cell given an absorbed photon (regardless of whether the photon is photoelectrically absorbed or not). By comparing these two curves, one can deconvolute effects of extrinsic device design (cell shading, anti-reflection coating, and back surface reflectors) from intrinsic device design (doping levels, surface recombination, carrier lifetimes, etc.).

$$IQE\{\lambda\}=\frac{EQE\{\lambda\}\cdot(1\text{-}R\{\lambda\})}{1\text{-}(T\{\lambda\}+R\{\lambda\})} \tag{13}$$

Samples G251815-W06 and G260605-W02 demonstrated in Figure 31 show EQE for the best quantum efficiency stabilization vs. temperature and highest EQE vs. temperature, respectively. Both units demonstrate a linear bandgap-temperature relationship of -0.4 meV/ °C with a residual fit of R^2=0.996. The similarity between the two samples ends here.
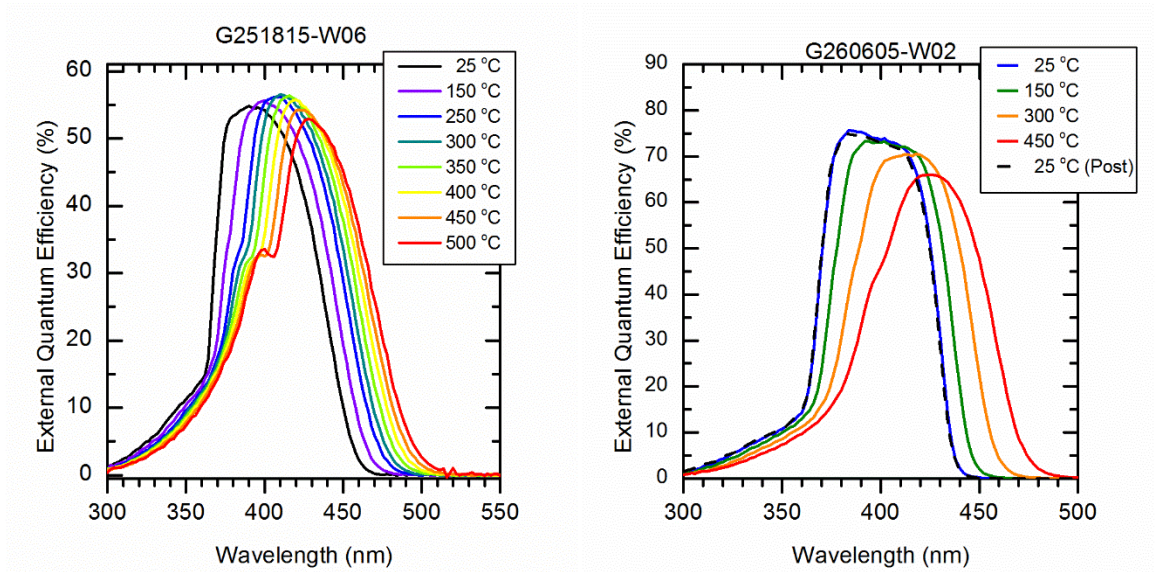
Figure 31. External quantum efficiency measurements versus temperature for the best temperature stability and highest absolute quantum efficiency.

Sample G251815-W06, demonstrating temperature resilience, has a peak EQE in the mid 50% range. Peak EQE values increase with temperature to about 300 °C

after which peak values begin decreasing with temperature. This is attributed to increased thermal escape from the quantum wells, and was expected. The turn-over is attributed to any number of deleterious effects of temperature overtaking the positive effects of thermal escape and is not surprising. Additionally, a shoulder on the blue response takes form and begins to impact performance more and more drastically. This is attributed to thermally activated donor-accepter pairs in the p-type GaN, and should occur at 3.27 eV (380 nm) at room temperature. [142] This absorption is in an "electrically dead" region and thus the activation of this mechanism reduces EQE.

Sample G260605-W02 shows a room temperature EQE that exceeds G251815-W06 by 20% absolute. However, this sample shows no initial increase in EQE, only a steady decline with temperature. That being said, it demonstrates higher EQE at any temperature than its counterpart. Serendipitously, G260605-W06 was retested at room temperature with nearly identical results as the original room temperature measurement indicating that the temperature cycle to 450 °C had no lasting effects on the device.
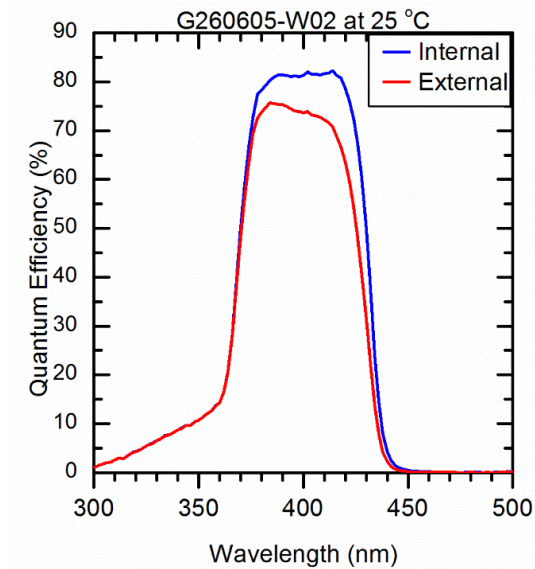
Figure 32. Comparison of Internal and External QE at room temperature.

The IQE curve, generated using Equation (13), gives more depth to the story of losses in quantum effeciency. The delta region between internal and external represents light that was either reflected our transmitted. This light can be successfully converted to electricity by reflection engineering (ARC and back reflectors) which has not yet been optimized in this project. The flat peak of the IQE is indicative of a layer that is acting as a neutral density filter [143], either the grid fingers or micro metallic regions of the ITO. The blue region, below E_G^{GaN}, is nearly identical between IQE and EQE. This suggests that the light is absorbed in the p-GaN layer and minority carriers electrons recombine long before they can diffuse to the junction.

ONE-SUN I-V PERFORMANCE

I-V measurements are used to measure the current through a device as a function of voltage. These measurements are performed in the dark and under illumination (both 1-Sun and multiple sun) as well as versus temperature. These

measurements show the nature of the diode behavior, V_{OC}, J_{SC}, FF, maximum power, and efficiency. The best I-V (and P-V) curves are displayed below with detailed analysis and meaning of all curve components.
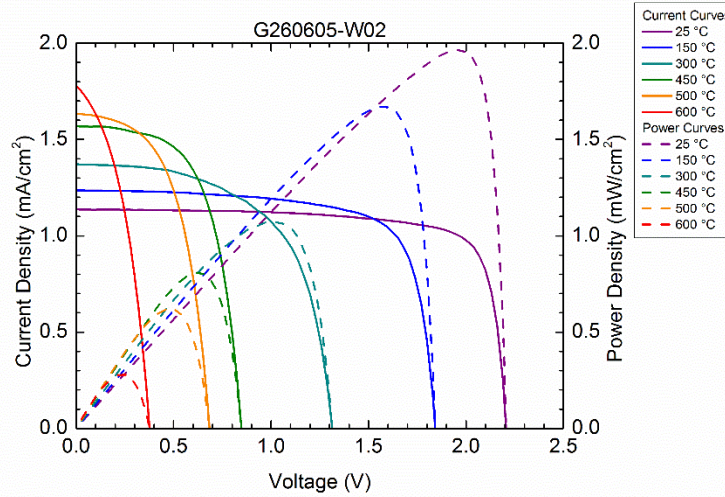
Figure 33. 1-Sun J-V and and PV curves for sampe G260605. Temperatures are color coded from purple (coldest) to red (hottest). Solid lines represent current, while dashed lines represent power.

The J-V curves displayed in Figure 33 represent the performance of the champion EQE cell G260605-W02. The cells show a steadily decreasing V_{oc} with temperature, in general this is to be expected. However, the rate of the decrease is much faster than the band gap narrowing (as extracted from EQE). The J_{SC} steadily increases with temperature, and based on the EQE results it can be deduced that this increase is solely due to the absorption edge shifting into the solar spectrum and not increased carrier collection. Fill factors steadily decrease with increasing temperature due to increased series resistance and decreased shunt resistance, this is to be expected with temperature.[144] All of these as well as other values are summarized in Table 7 below.

Table 7

1-Sun I-V Performance Metrics of G260605-W02 vs. Temperature

Temp. (°C)	E_G (eV)	V_{OC} (V)	W_{OC} (V)	J_{SC} (mA/cm^2)	Max. Pwr. (mW/cm^2)	FF (%)
25	2.87	2.20	0.67	1.13	1.96	79
150	2.82	1.84	0.98	1.23	1.67	74
300	2.75	1.31	1.44	137	1.07	60
450	2.67	0.84	1.84	1.57	0.81	61
500	2.66	0.68	1.98	1.63	0.62	56
600	2.62	0.38	2.24	1.78	0.28	41
Δ/°C x10^{-3}	-0.46	-3.21	2.76	1.13	-2.89	-0.57

TOPPING CELL CONCLUSIONS

The design, growth, fabrication, and characterization of a MQW InGaN solar cell has been demonstrated in this chapter and the results are very interesting. The use of this material and device architecture has shown the applicability of III-N's for construction of a high-temperature photovoltaic device. A cell with a V_{oc} of 2.20 V at room temperature at room temperature has shown 2.67 V at 450 °C and 0.38 V at 600 °C. Even though is performance is several degraded, it is quite significant to note that there is still a slight diode behavior and the device is not completely shunted. This is shown by a fill factor greater than 25%.

In the literature most cells are not tested at elevated temperatures, and even the ones that are don't exceed 200 °C. [56], [137], [140], [145] Meanwhile, the cell demonstrated in this chapter continues to perform up to 600 °C and has room temperature one-sun performance comparable to many of the individual cell metric record holders. Figure 34 plots the FOCUS cell against the cells for best efficiency [60], W_{OC} [56], [146], QC [61], and best FF [147]. While the FOCUS cell does not

directly exceed any of these cells it is tied with or right behind every other cell simultaneously.
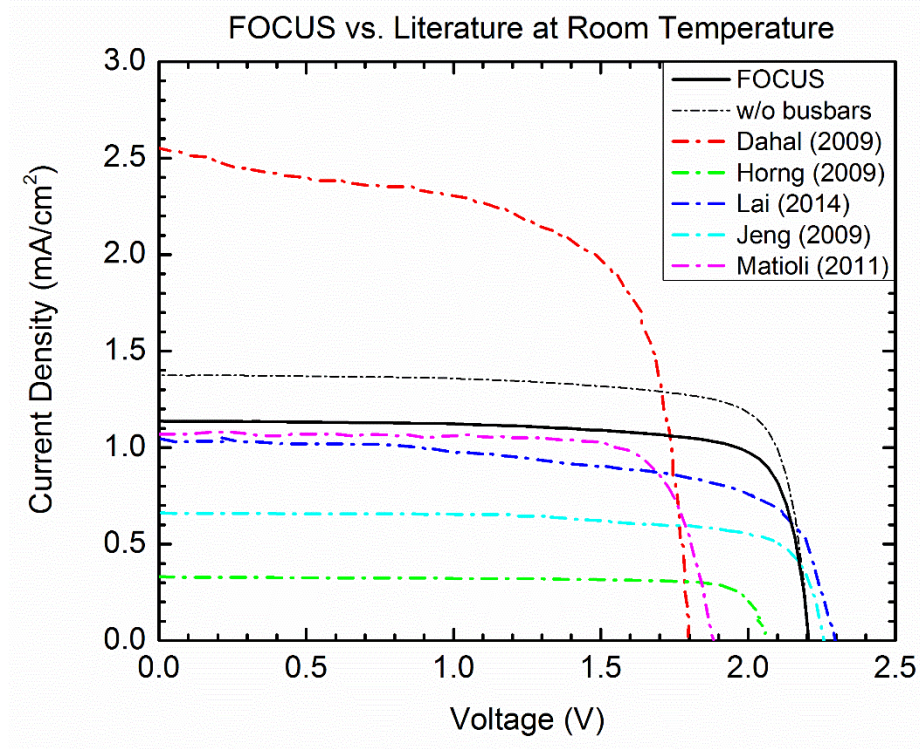
Figure 34. A comparison of 1-sun I-V curves of the FOCUS cell against champion cells from the literature.

The performance of this cell in the realm of InGaN-based solar cells is very promising, especially since the project will continue on after this thesis. There is obvious room for improvement that should be expanded upon. The most obvious is in the blue response, which can be improved through an inverted growth where by illumination will occur through the n-GaN (free of the highly recombination active Mg doping). An inverted structure will have the same series resistance through the thick n-GaN base region as the current cell, however, it will can have significantly reduced p-GaN series resistance. This will be possible through complete backside metallization of the p-GaN, ultimately removing the need for ITO. Considering another year of

development in this project, there is ample room for improvement in QC leading to a

higher overall efficiency.

CHAPTER 9

CONCLUSION AND FINAL REMARKS

The need for abundant and clean power is necessary to the continuation of human existence, and no power source is more abundant, and few are as clean as solar power. Though solar power is nearing market competitiveness on sunny days, it must beat all market expectations for it to be economically dominant in all climates. The silver bullet for solar power is to increase efficiency in the face of long entrenched ideology about low fundamental limits (~30%). This can be done by designing and building new types of photovoltaic devices operating outside the bounds of those fundamental parameters, though that will require new material technologies.

The III-N materials (AlN, GaN, InN, and their alloys) are a system of materials that have been implemented with revolutionary results in lighting and power electronics, and show similar promise for the field of solar technology. These materials with their widely tunable band gap (3.4 to 0.7 eV), range of carrier mobilities (300 to 2000 cm^2/V-s), strong absorption coefficient (10^6 /cm), and many other properties make them ideal for construction of many types of solar cells: multijunction, inversion junction, hot carrier cell, and carrier selective contact cell to name a few. All of these advantages indeed make studying the III-N system valuable for solar, however there are materials challenges that have previously prevented the commercialization of III-N based solar technology.

These materials have challenges stemming with epitaxy/mismatched substrates, thermodynamics of alloying, and spontaneous polarization. The lack of a native nitride substrate at reasonable cost means that hetero-epitaxy on foreign substrates generates massive defect densities (>10^9 / cm^2). Thermodynamic

84

equilibrium for the vast majority of the $In_xGa_{1-x}N$ alloy exists within a miscibility gap, and thus most of the compositions of $In_xGa_{1-x}N$ relevant to solar work are only metastable and must be created in challenging kinetically dominated growth regimes. Finally, the spontaneous polarization associated with the wurtzite crystal structure and the piezoelectric field from strain create fields and sheet charges in the material that may block or enhance carrier collection. Despite these challenges many have tried to construct a III-N device.

The construction of nitride solar cells has been investigated by many groups starting in 2007. Fabrication of devices was performed in either MOVPE or MBE reactors. While some homojunction p-n InGaN devices have been built the vast majority of devices involve an InGaN absorber sandwiched between p- and n- GaN to form a heterojunction. These iterations are further broken into bulk InGaN and InGaN-GaN MQW. Nearly all devices are grown on insulating sapphire substrates and thus must be fabricated into mesa structures. These devices have widely varying performances. Some cases show V_{OC}'s approaching or at the theoretical maximum for a given device, however in no cases are J_{SC}'s even close to their theoretical maximum. This means that InGaN devices classically suffer from either layers too thin for absorption, transport/recombination problems, or both. This thesis sought to explore many of these problems

One of the keys to developing new III-N devices is to revolutionize the methods by which nitride materials are grown such that many of the challenges associated with film synthesize can be overcome. Most of the material results demonstrated in this paper came from a nitride MBE system. However, unlike typical plasma-assisted MBE systems this tool used a novel nitrogen source. This revolves around a laser

sustained plasma in an antechamber. By focusing the laser—and thus location of the plasma—into the inlet of a supersonic nozzle, a collimated beam of N and Ar atoms is projected into the main MBE chamber towards the surface. This beam has the unique properties that the species are mostly monatomic, have energies between 0.5-2 eV, and flux densities greater than anything achievable with coulombic charged ions. This allows for higher growth rates, suppressed growth temperatures, and suppressed atom desorption. All other aspects of the chamber are similar to normal MBE chambers. These methods were used to grow III-N crystalline films in new regimes, however new device structures were also implemented to maximize the options for new breakthroughs.

The first method for advancing the field of solar with III-N material was in the area of carrier selective contacts to silicon. HIT cells currently dominant this technology by producing very good passivation, and thus high minority carrier lifetimes yielding world record voltages for silicon. These devices suffer from parasitic absorption by the surface ITO and a-Si. We have explored the possibility of using GaN to replace one or both of these layers since GaN has a higher band gap giving it a lower parasitic absorption. An analysis of band alignments using Anderson's models suggests GaN will make an excellent electron selective contact to silicon. GaN has been grown on Si at a range of temperature and with and without a-Si. We have determined that with current growth recipes GaN cannot passivate Si. However, the application of GaN to a thin layer of a-Si does little to affect the minority carrier lifetimes in the bulk and can still be used a replacement for ITO assuming its transport properties are high enough. This venue of exploration might still be fruitful,

however with little to gain and relatively high competition from many other potential CSC materials it is unlikely that further research occurs.

Building upon the idea of surface passivation the next concept explored was that of an inversion junction InGaN solar cell. This device would use a stack consisting of p-GaN/i-AlN/n-InGaN. The AlN would prevent the creation of a depletion region and the coulombic charges associated with the GaN and piezoelectric fields would be great enough to put the InGaN near the AlN-InGaN interface into inversion. This would induce a junction in the InGaN and no p-type InGaN would be needed. We have shown this process through modeling. Subsequent film growths have experimentally demonstrated optical and structural material quality for this type of structure. However, in general material quality still proved to be low, and thus research was shifted to advancing the quality of material.

The first step to creating good material from heteroepitaxial growth on a non-native substrate, w to develop a proper buffer technology. This was done through use of AlN growth on a nitridized sapphire surface. This technique yielded significantly lower TDD in the buffer layer from the previous chapter. Additionally, a process for smoothing nitride binaries was developed based on migration-enhanced epitaxy. This provided a strong foundation for subsequent nitride growth research.

Another potential candidate for new III-N device technology that was explored was bulk InN on a high-quality AlN buffer. This is of interest for use as an absorber material in a hot carrier solar cell. InN is theorized to be an ideal absorber and reservoir material for hot carrier solar cells as it has a small optical band gap and large phonon band gap, meaning it can absorb a large fraction of the solar spectrum and retain the carriers at excited states. We have shown material quality with

relatively low defect densities and at thickness necessary to absorb >90% of the incident solar spectrum. Continued research in the area will require further improving the material quality, confirming the theory of extended hot carrier lifetimes, and development of a selective energy contact (likely a resonant tunneling diode).

The next effort was to increase III-N growth speeds to make growth of III-N solar cells by MBE commercially relevant. This was done using the high flux ENABLE nitrogen source and a standard Ga cell to produce GaN. Films were grown at rates in excess of 3 µm/hr, and were comparable to industrial grade GaN by XRD and luminescence. These growth rates were limited by Ga flux long before nitrogen flux and thus should be able to go up to 5x faster.

The work culminated in the development of an InGaN MQW solar cell for refractory applications. These cells were designed to operate at 450 °C and were shown to be operable as solar cell up to 600 °C. Operation of a solar cell at these temperatures is unparalleled. This cell will ultimately be used for hybridization with concentrated solar thermal plants such that plants can increase their efficiency. By increasing plant efficiency, the cells will be able to lower plant LCOE making solar power more affordable. Through efficient management of the solar spectrum the InGaN will produce electricity while the thermal storage charges during the day. Thus providing cheap electricity at night as well as day.

FUTURE WORK AND FINAL REMARKS

This thesis has demonstrated many pathways forward for III-N technologies in the field of photovoltaics. Many of these paths forward are made possible through

the use of the ENABLE technology demonstrated in this thesis. While access to the ENABLE source technology is likely to be limited to non-existent here-to-forward, alternate paths do exist. Firstly, it should be possible to replicate the source technology on a new tool using the information within this thesis. Secondly, many of the advances demonstrated can be furthered without the use of the ENABLE source technology. These include but are not limited to advances in hot carrier solar cell technologies, GaN growth speeds, growth of high quality InGaN, and further engineering of refractory grade InGaN MQW solar cells.

The work displayed in this thesis demonstrated promising results for thick InN with high quality photoactive properties. Recent efforts by collaborators have shown this material to have a slight hot carrier effect [148]. Continuation of this work should focus on the development of an RTD as a selective energy contact. This is conceivably possible with GaN-GaN or GaN-InGaN layers and should make possible a full scale hot carrier solar cell device.

However, the subject of most interest to further work would be further developing the InGaN MQW cell for high temperature applications. The low hanging fruit for improving this work is all based around increasing the quantum efficiency of this device. The QE of above band gap photons is only at approximately one third; mature devices are closer to 90%. Obvious areas for improvements are in increasing absorption and extraction in the MQW. Pathways forward for this involve combing a number of different features, all with promising EQE, that were demonstrated independently: triangular doping profiles through the well-barrier, isothermal well barrier growth, optimized well and barrier thicknesses, and increasing the number of MQW without increasing defects. Additionally, current lost due to absorption in the

p-GaN can be mitigated, and this can result in an increase in J$_{SC}$ of up to 1 mA/cm^2. Improvements in the p-GaN can be achieved through optimization of doping profiles in conjunction with optimization of thickness. Though all of these optimizations are growth intensive and hence explain why they were not included in this thesis. A final method for increasing current from the wavelength absorbed in the p-GaN, is to invert the structure. This will require lift-off and transfer of the layer stack or intricate fabrication of devices with illumination through the sapphire substrate. The final area for improving this structure comes in the form of increasing the In:Ga ratio in the quantum well, however this is challenging and should not be undertaken lightly.

As final remarks emphasis should be placed on three topics from this thesis. First, it should be stated that the ENABLE source was a very unique way of creating reactive nitrogen that had room for growth into new forms of crystal growth. It is a shame that the technique has fallen by the wayside, however should it be reincarnated on a new tool the possibilities for new growth research are truly inspiring. Second, the promise of the nitrides is real. They have so much potential to do great things for the field of photovoltaics; they just need to be applied to the proper applications. As such, they should continue to be researched for this application. Finally, the potentials of solar to distribute, democratize, and reduce the cost of power production across the world have yet to be truly realized. Yet these potentials are too great to give up on, and efforts to advance solar technologies in the form of nitrides or other materials should continue to the benefit of all mankind.

REFERENCES

[1]   C. Pasten and J. C. Santamarina, "Energy and quality of life," *Energy Policy*, vol. 49, pp. 468–476, Oct. 2012.

[2]   International Energy Agency, *Solar Energy Perspectives*. 2011.

[3]   IEA, "Key World Energy Statistics 2014," 2014.

[4]   W. Shockley and H. J. Queisser, "Detailed balance limit of efficiency of p-n junction solar cells," *J. Appl. Phys.*, vol. 32, pp. 510–519, 1961.

[5]   G. Conibeer, "Third-generation photovoltaics," *Mater. Today*, vol. 10, no. 11, pp. 42–50, Nov. 2007.

[6]   M. A. Green, *Third Generation Photovoltaics*, vol. 12. Sydney, NSW, Australia: Springer Berlin Heidelberg, 2006.

[7]   R. F. Davis, "III-V nitrides for electronic and optoelectronic applications," *Proc. IEEE*, vol. 79, no. 5, pp. 702–712, May 1991.

[8]   I. Vurgaftman, J. R. Meyer, and L. R. Ram-Mohan, "Band parameters for III-V compound semiconductors and their alloys," *J. Appl. Phys.*, vol. 89, pp. 5815–5875, 2001.

[9]   S. C. Jain, M. Willander, J. Narayan, and R. Van Overstraeten, "III–nitrides: Growth, characterization, and properties," *J. Appl. Phys.*, vol. 87, p. 965, 2000.

[10]   S. Strite, "GaN, AlN, and InN: A review," *J. Vac. Sci. Technol. B Microelectron. Nanom. Struct.*, vol. 10, no. 4, p. 1237, Jul. 1992.

[11]   T. L. Tansley and C. P. Foley, "Optical band gap of indium nitride," *J. Appl. Phys.*, vol. 59, no. 9, p. 3241, 1986.

[12]   V. Y. Davydov, a. a. Klochikhin, R. P. Seisyan, V. V. Emtsev, S. V. Ivanov, F. Bechstedt, J. Furthmüller, H. Harima, a. V. Mudryi, J. Aderhold, O. Semchinova, and J. Graul, "Absorption and emission of hexagonal InN. Evidence of narrow fundamental band gap," *phys. stat. sol.*, vol. 229, no. 3, pp. 1972–1974, 2002.

[13]   J. Wu, W. Walukiewicz, K. M. Yu, J. W. Ager, E. E. Haller, H. Lu, W. J. Schaff, Y. Saito, and Y. Nanishi, "Unusual properties of the fundamental band gap of InN," *Appl. Phys. Lett.*, vol. 80, pp. 3967–3969, 2002.

[14]   J. Wu, W. Walukiewicz, K. Yu, and J. A. Iii, "Indium nitride: A narrow gap semiconductor," *Info:*, pp. 1–8, 2002.

[15]   J. Nelson, *The Physics of Solar Cells*. 2003.

[16] K. Xu and A. Yoshikawa, "Effects of film polarities on InN growth by molecular-beam epitaxy," *Appl. Phys. Lett.*, vol. 83, no. 2, pp. 251–253, 2003.

[17] A. G. Bhuiyan, K. Sugita, K. Kasashima, A. Hashimoto, A. Yamamoto, and V. Y. Davydov, "Single-crystalline InN films with an absorption edge between 0.7 and 2 eV grown using different techniques and evidence of the actual band gap energy," *Appl. Phys. Lett.*, vol. 83, no. 23, p. 4788, 2003.

[18] K. S. A. Butcher, M. Wintrebert-Fouquet, P. P.-T. Chen, H. Timmers, and S. K. Shrestha, "Detailed analysis of absorption data for indium nitride," *Mater. Sci. Semicond. Process.*, vol. 6, no. 5–6, pp. 351–354, Oct. 2003.

[19] R. Gergova, K. S. A. Butcher, P. W. Binsted, and D. Gogova, "Initial results for epitaxial growth of InN on gallium oxide and improved Migration-Enhanced Afterglow Epitaxy growth on gallium nitride," *J. Vac. Sci. Technol. B*, vol. 32, no. May, p. 031207, 2014.

[20] G. Franssen, I. Gorczyca, T. Suski, A. Kamińska, J. Pereiro, E. Muñoz, E. Iliopoulos, A. Georgakilas, S. B. Che, Y. Ishitani, A. Yoshikawa, N. E. Christensen, and A. Svane, "Bowing of the band gap pressure coefficient in In[sub x]Ga[sub 1−x]N alloys," *J. Appl. Phys.*, vol. 103, no. 3, p. 033514, 2008.

[21] D. Brunner, H. Angerer, E. Bustarret, F. Freudenberg, R. Höpler, R. Dimitrov, O. Ambacher, and M. Stutzmann, "Optical constants of epitaxial AlGaN films and their temperature dependence," *J. Appl. Phys.*, vol. 82, no. 10, p. 5090, 1997.

[22] R. E. Jones, R. Broesler, K. M. Yu, J. W. Ager, E. E. Haller, W. Walukiewicz, X. Chen, and W. J. Schaff, "Band gap bowing parameter of In[sub 1−x]Al[sub x]N," *J. Appl. Phys.*, vol. 104, no. 12, p. 123501, 2008.

[23] H. Morkoç, *Nitride Semiconductors and devices*, 1st ed. Berlin: Springer, 1999.

[24] J. F. Muth, J. H. Lee, I. K. Shmagin, R. M. Kolbas, H. C. Casey, B. P. Keller, U. K. Mishra, and S. P. DenBaars, "Absorption coefficient, energy gap, exciton binding energy, and recombination lifetime of GaN obtained from transmission measurements," *Appl. Phys. Lett.*, vol. 71, no. 18, pp. 2572–2574, 1997.

[25] H. C. Casey, D. D. Sell, and K. W. Wecht, "Concentration dependence of the absorption coefficient for n− and p−type GaAs between 1.3 and 1.6 eV," *J. Appl. Phys.*, vol. 46, no. 1, p. 250, 1975.

[26] S. Adachi, "Optical dispersion relations for GaP, GaAs, GaSb, InP, InAs, InSb, AlxGa1−xAs, and In1−xGaxAsyP1−y," *J. Appl. Phys.*, vol. 66, no. 12, p. 6030, 1989.

[27] A. V. Davydov and T. J. Anderson, *Proceedings of the Third Symposium on*

III-V Nitride Materials and Processes. Pennington, NJ: Electrochemical Society, 1998.

[28]   L. Berger, *Semiconductor Materials*. Boca Raton: CRC Press, 1997.

[29]   C. a. Tran, A. Osinski, R. F. Karlicek, and I. Berishev, "Growth of InGaN/GaN multiple-quantum-well blue light-emitting diodes on silicon by metalorganic vapor phase epitaxy," *Appl. Phys. Lett.*, vol. 75, no. 11, p. 1494, 1999.

[30]   S.-H. Chang, Y.-K. Fang, S.-F. Ting, C.-Y. Lin, S.-F. Chen, H. Kuan, and C.-Y. Liang, "Poly- and single-crystalline h-GaN grown on SiCN/Si(100) and SiCN/Si(111) substrates by MOCVD," *J. Electron. Mater.*, vol. 35, no. 10, pp. 1837–1841, Oct. 2006.

[31]   I. Ho and G. B. Stringfellow, "Solid phase immiscibility in GaInN," *Appl. Phys. Lett.*, vol. 2701, no. 18, pp. 2701–2703, 1996.

[32]   T. D. Moustakas, "The role of extended defects on the performance of optoelectronic devices in nitride semiconductors," *Phys. status solidi*, vol. 210, no. 1, pp. 169–174, Jan. 2013.

[33]   G. E. Moore, "Direct Observation of the Thermal Dissociation of Molecular Nitrogen," *J. Chem. Phys.*, vol. 54, no. 1, p. 399, 1971.

[34]   A. H. White and W. Melville, "The Decomposition of Ammonia at High Temperatures," *J. Am. Chem. Soc.*, vol. 27, no. 4, pp. 373–386, Apr. 1905.

[35]   C. Skierbiszewski, "From high electron mobility GaN/AlGaN heterostructures to blue-violet InGaN laser diodes. perspectives of MBE for nitride optoelectronics," *Acta Phys. Pol. Ser. a*, vol. 108, no. 4, pp. 635–651, 2005.

[36]   R. Averbeck and H. Riechert, "Quantitative Model for the MBE-Growth of Ternary Nitrides," *Phys. status solidi*, vol. 176, no. 1, pp. 301–305, Nov. 1999.

[37]   V. Cimalla, V. Lebedev, F. M. Morales, M. Niebelschütz, G. Ecke, R. Goldhahn, and O. Ambacher, "Origin of n-type conductivity in nominally undoped InN," *Materwiss. Werksttech.*, vol. 37, no. 11, pp. 924–928, Nov. 2006.

[38]   J. Neugebauer and C. G. Van de Walle, "Gallium vacancies and the yellow luminescence in GaN," *Appl. Phys. Lett.*, vol. 69, p. 503, 1996.

[39]   W. Götz, N. M. Johnson, C. Chen, H. Liu, C. Kuo, and W. Imler, "Activation energies of Si donors in GaN," *Appl. Phys. Lett.*, vol. 68, no. 22, pp. 3144–3146, 1996.

[40]   S. Fischer, C. Wetzel, E. E. Haller, and B. K. Meyer, "On p-type doping in GaN—acceptor binding energies," *Appl. Phys. Lett.*, vol. 67, no. 9, p. 1298, 1995.

[41] Isamu Akasaki, Hiroshi Amano, Masahiro Kito, and Kazumasa Hiramatsu, "Photoluminescence of Mg-doped p-type GaN and electroluminescence of GaN p-n junction LED," *J. Lumin.*, vol. 48–49, pp. 666–670, Jan. 1991.

[42] K. Kumakura, T. Makimoto, and N. Kobayashi, "Mg-acceptor activation mechanism and transport characteristics in p-type InGaN grown by metalorganic vapor phase epitaxy," *J. Appl. Phys.*, vol. 93, pp. 3370–3375, 2003.

[43] S. J. Pearton, J. C. Zolper, R. J. Shul, and F. Ren, "GaN: Processing, defects, and devices," *J. Appl. Phys.*, vol. 86, no. 1, p. 1, 1999.

[44] A. Feduniewicz, C. Skierbiszewski, M. Siekacz, Z. R. Wasilewski, I. Sproule, S. Grzanka, R. Jakieła, J. Borysiuk, G. Kamler, E. Litwin-Staszewska, R. Czernecki, M. Boćkowski, and S. Porowski, "Control of Mg doping of GaN in RF-plasma molecular beam epitaxy," *J. Cryst. Growth*, vol. 278, no. 1–4, pp. 443–448, May 2005.

[45] W. Götz, N. M. Johnson, J. Walker, and D. P. Bour, "Activation of Acceptors in Mg-Doped, p-Type GaN," *MRS Proc.*, vol. 423, p. 595, Jan. 1996.

[46] R. R. King, D. Bhusari, A. Boca, D. Larrabee, X.-Q. Liu, W. Hong, C. M. Fetzer, D. C. Law, and N. H. Karam, "Band gap-voltage offset and energy production in next-generation multijunction solar cells," *Prog. Photovoltaics Res. Appl.*, vol. 19, no. 7, pp. 797–812, Nov. 2011.

[47] S. A. Ringel, J. A. Carlin, C. L. Andre, M. K. Hudait, M. Gonzalez, D. M. Wilt, E. B. Clark, P. Jenkins, D. Scheiman, A. Allerman, E. A. Fitzgerald, and C. W. Leitz, "Single-junction InGaP/GaAs solar cells grown on Si substrates with SiGe buffer layers," *Prog. Photovoltaics Res. Appl.*, vol. 10, no. 6, pp. 417–426, Sep. 2002.

[48] A. E. Chernyakov, M. M. Sobolev, V. V. Ratnikov, N. M. Shmidt, and E. B. Yakimov, "Nonradiative recombination dynamics in InGaN/GaN LED defect system," *Superlattices Microstruct.*, vol. 45, no. 4–5, pp. 301–307, Apr. 2009.

[49] A. G. Bhuiyan, K. Sugita, A. Hashimoto, and A. Yamamoto, "InGaN Solar Cells: Present State of the Art and Important Challenges," *IEEE J. Photovoltaics*, vol. 2, no. 3, pp. 276–293, Jul. 2012.

[50] J. Wu, W. Walukiewicz, K. M. Yu, W. Shan, J. W. Ager, E. E. Haller, H. Lu, W. J. Schaff, W. K. Metzger, and S. Kurtz, "Superior radiation resistance of In 1-xGa xN alloys: Full-solar-spectrum photovoltaic material system," *J. Appl. Phys.*, vol. 94, no. 10, pp. 6477–6482, 2003.

[51] O. Jani, I. Ferguson, C. Honsberg, and S. Kurtz, "Design and characterization of GaNInGaN solar cells," *Appl. Phys. Lett.*, vol. 91, no. 13, pp. 13–15, 2007.

[52] O. Jani, H. Yu, E. Trybus, B. Jampana, I. Ferguson, A. Doolittle, and C.

Honsberg, "Effect of Phase Seperation on Performance on III V Nitride Solar Cells," *22nd Eur. Photovolt. Sol. Energy Conf.*, no. September, pp. 64–67, 2007.

[53]   C. Yang, X. X. Wang, H. Xiao, J. Ran, C. Wang, G. Hu, X. X. Wang, X. Zhang, J. J. Li, and J. J. Li, "Photovoltaic effects in InGaN structures with p-n junctions," *Phys. Status Solidi Appl. Mater.*, vol. 204, no. 12, pp. 4288–4291, 2007.

[54]   S. W. Zeng, B. P. Zhang, J. W. Sun, J. F. Cai, C. Chen, and J. Z. Yu, "Substantial photo-response of InGaN p–i–n homojunction solar cells," *Semicond. Sci. Technol.*, vol. 24, no. 5, p. 055009, 2009.

[55]   C. Boney, I. Hernandez, R. Pillai, D. Starikov, A. Bensaoula, M. Henini, M. Syperek, J. Misiewicz, and R. Kudrawiec, "Growth and characterization of InGaN for photovoltaic devices," *Phys. status solidi*, vol. 8, no. 7–8, pp. 2460–2462, Jul. 2011.

[56]   M.-J. Jeng, Y.-L. Lee, and L.-B. Chang, "Temperature dependences of In x Ga 1− x N multiple quantum well solar cells," *J. Phys. D. Appl. Phys.*, vol. 42, no. 10, p. 105101, May 2009.

[57]   K. Y. Lai, G. J. Lin, Y.-L. Lai, Y. F. Chen, and J. H. He, "Effect of indium fluctuation on the photovoltaic characteristics of InGaN/GaN multiple quantum well solar cells," *Appl. Phys. Lett.*, vol. 96, no. 8, p. 081103, 2010.

[58]   Y.-J. Lee, M.-H. Lee, C.-M. Cheng, and C.-H. Yang, "Enhanced conversion efficiency of InGaN multiple quantum well solar cells grown on a patterned sapphire substrate," *Appl. Phys. Lett.*, vol. 98, no. 2011, p. 263504, 2011.

[59]   R. Dahal, J. Li, K. Aryal, J. Y. Lin, and H. X. Jiang, "InGaN/GaN multiple quantum well concentrator solar cells," *Appl. Phys. Lett.*, vol. 97, no. 7, p. 073115, 2010.

[60]   R. Dahal, B. Pantha, J. Li, J. Y. Lin, and H. X. Jiang, "InGaN/GaN multiple quantum well solar cells with long operating wavelengths," *Appl. Phys. Lett.*, vol. 94, no. 6, p. 063505, 2009.

[61]   E. Matioli, C. Neufeld, M. Iza, S. C. Cruz, A. A. Al-Heji, X. Chen, R. M. Farrell, S. Keller, S. DenBaars, U. Mishra, S. Nakamura, J. Speck, and C. Weisbuch, "High internal and external quantum efficiency InGaN/GaN solar cells," *Appl. Phys. Lett.*, vol. 98, no. 2, pp. 3–5, 2011.

[62]   M. A. Green, K. Emery, Y. Hishikawa, W. Warta, and E. D. Dunlop, "Solar cell efficiency tables (version 46)," *Prog. Photovoltaics Res. Appl.*, vol. 23, no. 7, pp. 805–812, Jul. 2015.

[63]   M. Z. Kauser, A. Osinsky, a. M. Dabiran, and S. J. Pearton, "Optimization of conductivity in p-type GaN/InGaN-graded superlattices," *J. Appl. Phys.*, vol.

97, no. 8, p. 083715, 2005.

[64]   C. J. Neufeld, N. G. Toledo, S. C. Cruz, M. Iza, S. P. DenBaars, and U. K. Mishra, "High quantum efficiency InGaN/GaN solar cells with 2.95 eV band gap," *Appl. Phys. Lett.*, vol. 93, no. 14, pp. 14–17, 2008.

[65]   X. Zheng, R. H. Horng, D. S. Wuu, M. T. Chu, W. Y. Liao, M. H. Wu, R. M. Lin, and Y. C. Lu, "High-quality InGaN/GaN heterojunctions and their photovoltaic effects," *Appl. Phys. Lett.*, vol. 93, no. 2008, pp. 2006–2009, 2008.

[66]   T. Fujii, Y. Kuwahara, D. Iida, Y. Fujiyama, Y. Morita, T. Sugiyama, Y. Isobe, M. Iwaya, T. Takeuchi, S. Kamiyama, I. Akasaki, and H. Amano, "GaInN-based solar cells using GaInN/GaInN superlattices," *Phys. Status Solidi*, vol. 8, no. 7–8, pp. 2463–2465, 2011.

[67]   C. L. Tsai, G. S. Liu, G. C. Fan, and Y. S. Lee, "Substrate-free large gap InGaN solar cells with bottom reflector," *Solid. State. Electron.*, vol. 54, no. 5, pp. 541–544, 2010.

[68]   J.-P. Shim, M. Choe, S.-R. Jeon, D. Seo, T. Lee, and D.-S. Lee, "InGaN-Based p–i–n Solar Cells with Graphene Electrodes," *Appl. Phys. Express*, vol. 4, no. 5, p. 052302, 2011.

[69]   B. W. Liou, "Design and fabrication of In x Ga 1 − x N / GaN solar cells with a multiple-quantum-well structure on SiCN / Si (111) substrates," *Thin Solid Films*, vol. 520, no. 3, pp. 1–7, 2011.

[70]   W. E. Quinn, "Multi-Wafer Molecular Beam Epitaxy for High Performance p-hemts," in *Proceedings of the Symposium on High Speed III-V Electronics for Wireless Applications and the Twenty-Fifth State-of-the-Art Program on Compound Semiconductors*, 1996, pp. 22–28.

[71]   S. D. Burnham, W. Alan Doolittle, G. Namkoong, and W. Henderson, "Mg Doped GaN Using a Valved, Thermally Energetic Source: Enhanced Incorporation, Control and Quantitative Optimization," *MRS Proc.*, vol. 798, p. Y8.11, Jan. 2003.

[72]   M. Tanaka, M. Taguchi, T. Matsuyama, T. Sawada, S. Tsuda, S. Nakano, H. Hanafusa, and Y. Kuwano, "Development of New a-Si/c-Si Heterojunction Solar Cells: ACJ-HIT (Artificially Constructed Junction-Heterojunction with Intrinsic Thin-Layer)," *Jpn. J. Appl. Phys.*, vol. 31, no. Part 1, No. 11, pp. 3518–3522, Nov. 1992.

[73]   K. Masuko, M. Shigematsu, T. Hashiguchi, D. Fujishima, M. Kai, N. Yoshimura, T. Yamaguchi, Y. Ichihashi, T. Mishima, N. Matsubara, T. Yamanishi, T. Takahama, M. Taguchi, E. Maruyama, and S. Okamoto, "Achievement of More Than 25% Conversion Efficiency With Crystalline Silicon Heterojunction Solar Cell," *IEEE J. Photovoltaics*, vol. 4, no. 6, pp.

1433–1435, Nov. 2014.

[74] K. Ghosh, C. J. Tracy, S. Herasimenka, C. Honsberg, and S. Bowden, "Explanation of the device operation principle of amorphous silicon/ crystalline silicon heterojunction solar cell and role of the inversion of crystalline silicon surface," in *2010 35th IEEE Photovoltaic Specialists Conference*, 2010, pp. 001383–001386.

[75] K. Ghosh, S. Bowden, and C. Tracy, "Role of hot carriers in the interfacial transport in amorphous silicon/crystalline silicon heterostructure solar cells," *Phys. status solidi*, vol. 210, no. 2, pp. 413–419, Feb. 2013.

[76] Z. C. Holman, A. Descoeudres, L. Barraud, F. Z. Fernandez, J. P. Seif, S. De Wolf, and C. Ballif, "Current Losses at the Front of Silicon Heterojunction Solar Cells," *IEEE J. Photovoltaics*, vol. 2, no. 1, pp. 7–15, Jan. 2012.

[77] Z. C. Holman, A. Descoeudres, S. De Wolf, and C. Ballif, "Record Infrared Internal Quantum Efficiency in Silicon Heterojunction Solar Cells With Dielectric/Metal Rear Reflectors," *IEEE J. Photovoltaics*, vol. 3, no. 4, pp. 1243–1249, Oct. 2013.

[78] M. Taguchi, H. Sakata, Y. Yoshimine, E. Maruyama, A. Terakawa, M. Tanaka, and S. Kiyama, "An approach for the higher efficiency in the HIT cells," *Conf. Rec. Thirty-first IEEE Photovolt. Spec. Conf. 2005.*, 2005.

[79] F. Feldmann, M. Simon, M. Bivour, C. Reichel, M. Hermle, and S. W. Glunz, "Carrier-selective contacts for Si solar cells," *Appl. Phys. Lett.*, vol. 104, no. 18, p. 181105, May 2014.

[80] L. Ding, M. Boccard, J. Williams, A. Jeffries, S. Gangam, K. Ghosh, C. Honsberg, S. Bowden, Z. Holman, H. Atwater, T. Buonassisi, S. Bremner, M. Green, C. Ballif, and M. Bertoni, "'Thin silicon solar cells: A path to 35% shockley-queisser limits', a DOE funded FPACE II project," in *2014 IEEE 40th Photovoltaic Specialist Conference (PVSC)*, 2014, pp. 2467–2470.

[81]   a. Descoeudres, L. Barraud, S. De Wolf, B. Strahm, D. Lachenal, C. Guérin, Z. C. Holman, F. Zicarelli, B. Demaurex, J. Seif, J. Holovsky, and C. Ballif, "Improved amorphous/crystalline silicon interface passivation by hydrogen plasma treatment," *Appl. Phys. Lett.*, vol. 99, no. 12, p. 123506, 2011.

[82] H. Fujiwara and M. Kondo, "Impact of epitaxial growth at the heterointerface of a-Si:H/c-Si solar cells," *Appl. Phys. Lett.*, vol. 90, no. 1, p. 013503, 2007.

[83] L. Korte, E. Conrad, H. Angermann, R. Stangl, and M. Schmidt, "Advances in a-Si:H/c-Si heterojunction solar cell fabrication and characterization," *Sol. Energy Mater. Sol. Cells*, vol. 93, no. 6–7, pp. 905–910, Jun. 2009.

[84] A. Descoeudres, Z. C. Holman, L. Barraud, S. Morel, S. De Wolf, and C. Ballif, ">21% Efficient Silicon Heterojunction Solar Cells on n- and
97

p-Type Wafers Compared," *IEEE J. Photovoltaics*, vol. 3, no. 1, pp. 83–89, Jan. 2013.

[85] R. L. Anderson, "Germanium-Gallium Arsenide Heterojunctions [Letter to the Editor]," *IBM J. Res. Dev.*, vol. 4, no. 3, pp. 283–287, Jul. 1960.

[86] Z. Chen, W. Li, R. Li, Y. Zhang, G. Xu, and H. Cheng, "Fabrication of Highly Transparent and Conductive Indium–Tin Oxide Thin Films with a High Figure of Merit via Solution Processing," *Langmuir*, vol. 29, no. 45, pp. 13836–13842, Nov. 2013.

[87] R. L. Anderson, "Experiments on Ge-GaAs heterojunctions," *IRE Trans. Electron Devices*, vol. 9, no. 6, pp. 509–509, Nov. 1962.

[88] F. Flores and C. Tejedor, "Energy barriers and interface states at heterojunctions," *J. Phys. C Solid State Phys.*, vol. 12, no. 4, pp. 731–749, Feb. 1979.

[89] M. Ilegems and H. C. Montgomery, "Electrical Properties of n-type vapor-grown Gallium Nitride," *J. Phys. Chem. Solids*, vol. 34, pp. 885–895, 1973.

[90] R. K. Crouch, W. J. Debnam, and A. L. Fripp, "Properties of GaN grown on sapphire substrates," *J. Mater. Sci.*, vol. 13, no. 11, pp. 2358–2364, Nov. 1978.

[91] M. E. Levinshteǐn, S. L. Rumyantsev, and M. Shur, *Properties of advanced semiconductor materials*. New York: Wiley, 2001.

[92] T. Lei, M. Fanciulli, R. J. Molnar, T. D. Moustakas, R. J. Graham, and J. Scanlon, "Epitaxial growth of zinc blende and wurtzitic gallium nitride thin films on (001) silicon," *Appl. Phys. Lett.*, vol. 59, pp. 944–946, 1991.

[93] B. Gunning, J. Lowder, M. Moseley, and W. A. Doolittle, "Negligible carrier freeze-out facilitated by impurity band conduction in highly p-type GaN," *Appl. Phys. Lett.*, vol. 101, pp. 1–5, 2012.

[94] C. a M. Fabien, M. Moseley, B. Gunning, W. A. Doolittle, A. M. Fischer, Y. O. Wei, and F. a. Ponce, "Simulations, practical limitations, and novel growth technology for InGaN-based solar cells," *IEEE J. Photovoltaics*, vol. 4, pp. 601–606, 2014.

[95] E. Trybus, G. Namkoong, W. Henderson, S. Burnham, W. A. Doolittle, M. Cheung, and A. Cartwright, "InN: A material with photovoltaic promise and challenges," *J. Cryst. Growth*, vol. 288, no. 2, pp. 218–224, Mar. 2006.

[96] J. J. Williams, T. L. Williamson, M. a. Hoffbauer, A. M. Fischer, S. M. Goodnick, N. N. Faleev, K. Ghosh, and C. B. Honsberg, "Inducing a junction in n-type InxGa(1−x)N," *J. Vac. Sci. Technol. B Microelectron. Nanom. Struct.*, vol. 31, no. 3, p. 03C127, 2013.

[97] J.-R. Chen, C.-H. Lee, T.-S. Ko, Y.-A. Chang, T.-C. Lu, H.-C. Kuo, Y.-K. Kuo, and S.-C. Wang, "Effects of Built-In Polarization and Carrier Overflow on InGaN Quantum-Well Lasers With Electronic Blocking Layers," *J. Light. Technol.*, vol. 26, no. 3, pp. 329–337, 2008.

[98] T. L. Williamson, A. L. Salazar, J. J. Williams, and M. a. Hoffbauer, "Improvements in the compositional uniformity of In-rich InxGa1-xN films grown at low temperatures by ENABLE," *Phys. status solidi*, vol. 8, no. 7–8, pp. 2098–2100, Jul. 2011.

[99] N. Miller, R. E. Jones, K. M. Yu, J. W. Ager, Z. Liliental-Weber, E. E. Haller, W. Walukiewicz, T. L. Williamson, and M. a. Hoffbauer, "Low-temperature grown compositionally graded InGaN films," *Phys. status solidi*, vol. 5, no. 6, pp. 1866–1869, May 2008.

[100] T. L. Williamson, J. J. Williams, J. C. D. Hubbard, and M. a. Hoffbauer, "High In content In[sub x]Ga[sub 1−x]N grown by energetic neutral atom beam lithography and epitaxy under slightly N-rich conditions," *J. Vac. Sci. Technol. B Microelectron. Nanom. Struct.*, vol. 29, no. 3, p. 03C132, 2011.

[101] J. E. Ayers, "The measurement of threading dislocation densities in semiconductor crystals by X-ray diffraction," *J. Cryst. Growth*, vol. 135, no. 1–2, pp. 71–77, Jan. 1994.

[102] P. G. Moses and C. G. Van De Walle, "Band bowing and band alignment in InGaN alloys," *Appl. Phys. Lett.*, vol. 96, pp. 1–3, 2010.

[103] E. Zielińska-Rohozińska, J. Gronkowski, K. Pakula, M. Majer, M. Regulska, and L. Nowicki, "Strain relaxation in Ga1-xInxN thin layers grown on GaN sublayers," *J. Alloys Compd.*, vol. 328, pp. 199–205, 2001.

[104] V. Kirchner, R. Ebel, H. Heinke, S. Einfeldt, D. Hommel, H. Selke, and P. L. Ryder, "Influence of buffer layers on the structural properties of molecular beam epitaxy grown GaN layers," *Mater. Sci. Eng. B Solid State Mater. Adv. Technol.*, vol. 59, no. 1–3, pp. 47–51, 1999.

[105] Q. Sun, Y. S. Cho, I. H. Lee, J. Han, B. H. Kong, and H. K. Cho, "Nitrogen-polar GaN growth evolution on c-plane sapphire," *Appl. Phys. Lett.*, vol. 93, pp. 13–16, 2008.

[106] K. Sasamoto, T. Hotta, K. Sugita, a. G. Bhuiyan, a. Hashimoto, a. Yamamoto, K. Kinoshita, and Y. Kohji, "MOVPE growth of high quality p-type InGaN with intermediate in compositions," *J. Cryst. Growth*, vol. 318, no. 1, pp. 492–495, 2011.

[107] M. Takeuchi, H. Shimizu, R. Kajitani, K. Kawasaki, Y. Kumagai, A. Koukitu, and Y. Aoyagi, "Improvement of crystalline quality of N-polar AlN layers on c-plane sapphire by low-pressure flow-modulated MOCVD," *J. Cryst. Growth*,

vol. 298, no. SPEC. ISS, pp. 336–340, Jan. 2007.

[108] P. Ming-Zeng, G. Li-Wei, Z. Jie, Y. Nai-Sen, Z. Xue-Liang, Y. Jian-Feng, G. Bin-Hui, J. Hai-Qiang, C. Hong, and Z. Jun-Ming, "Three-Step Growth Optimization of AlN Epilayers by MOCVD," *Chinese Phys. Lett.*, vol. 25, no. 6, pp. 2265–2268, Jun. 2008.

[109] O. E. Contreras, F. Ruiz-Zepeda, A. Dadgar, A. Krost, and F. a. Ponce, "Atomic Arrangement at the AlN/Si(110) Interface," *Appl. Phys. Express*, vol. 1, p. 061104, Jun. 2008.

[110] M. S. Shur, "GaN based transistors for high power applications," *Solid. State. Electron.*, vol. 42, no. 12, pp. 2131–2138, Dec. 1998.

[111] T. Mukai, M. Yamada, and S. Nakamura, "Characteristics of InGaN-Based UV/Blue/Green/Amber/Red Light-Emitting Diodes," *Jpn. J. Appl. Phys.*, vol. 38, pp. 3976–3981, 1999.

[112] a. T. Schremer, J. a. Smart, Y. Wang, O. Ambacher, N. C. MacDonald, and J. R. Shealy, "High electron mobility AlGaN/GaN heterostructure on (111) Si," *Appl. Phys. Lett.*, vol. 76, no. 6, p. 736, 2000.

[113] X. Wang and A. Yoshikawa, "Molecular beam epitaxy growth of GaN, AlN and InN," *Prog. Cryst. Growth Charact. Mater.*, vol. 48–49, pp. 42–103, 2004.

[114] T. L. Williamson, M. a. Hoffbauer, K. M. Yu, L. a. Reichertz, M. E. Hawkridge, R. E. Jones, N. Miller, J. W. Ager, Z. Liliental-Weber, and W. Walukiewicz, "Highly luminescent InxGa1-xN thin films grown over the entire composition range by energetic neutral atom beam lithography & epitaxy (ENABLE)," *Phys. status solidi*, vol. 6, no. S2, pp. S409–S412, Jun. 2009.

[115] G. S. Solomon, J. A. Trezza, and J. S. Harris, "Effects of monolayer coverage, flux ratio, and growth rate on the island density of InAs islands on GaAs," *Appl. Phys. Lett.*, vol. 3161, no. May, p. 3161, 1995.

[116] T. Metzger, R. Hopler, E. Born, S. Christiansen, M. Albrecht, H. P. Strunk, and O. Ambacher, "Coherent X-Ray Scattering Phenomenon in Highly Disordered Epitaxial AlN Films," *Phys. Status Solidi*, vol. 162, no. 2, pp. 529–535, Aug. 1997.

[117] P. F. Miceli, C. J. Palmstrøm, and K. W. Moyers, "X-ray scattering study of lattice relaxation in ErAs epitaxial layers on GaAs," *Appl. Phys. Lett.*, vol. 58, no. 15, p. 1602, 1991.

[118] N. Faleev, H. Lu, and W. J. Schaff, "Low density of threading dislocations in AlN grown on sapphire," *J. Appl. Phys.*, vol. 101, no. 9, p. 093516, 2007.

[119] R. T. Ross, "Efficiency of hot-carrier solar energy converters," *J. Appl. Phys.*, vol. 53, no. 5, p. 3813, 1982.

[120] C. Bayram, D. K. Sadana, Z. Vashaei, and M. Razeghi, "Reliable GaN-based resonant tunneling diodes with reproducible room-temperature negative differential resistance," in *Proceeding of SPIE*, 2012, vol. 8268, pp. 826827–826827–9.

[121] G. J. Conibeer, D. König, M. A. Green, and J. F. Guillemoles, "Slowing of carrier cooling in hot carrier solar cells," *Thin Solid Films*, vol. 516, no. 20, pp. 6948–6953, Aug. 2008.

[122] N. Faleev, N. Sustersic, N. Bhargava, J. Kolodzey, S. Magonov, D. J. Smith, and C. Honsberg, "Structural investigations of SiGe epitaxial layers grown by molecular beam epitaxy on Si(001) and Ge(001) substrates: II—Transmission electron microscopy and atomic force microscopy," *J. Cryst. Growth*, vol. 365, pp. 35–43, Feb. 2013.

[123] N. Faleev, N. Sustersic, N. Bhargava, J. Kolodzey, A. Y. Kazimirov, and C. Honsberg, "Structural investigations of SiGe epitaxial layers grown by molecular beam epitaxy on Si(001) and Ge(001) substrates: I—High-resolution x-ray diffraction and x-ray topography," *J. Cryst. Growth*, vol. 365, pp. 44–53, Feb. 2013.

[124] P. F. Miceli and C. J. Palmstrom, "X-ray scattering from rotational disorder in epitaxial films: An unconventional mosaic crystal," *Phys. Rev. B*, vol. 51, no. 8, pp. 5506–5509, 1995.

[125] H. Heinke, V. Kirchner, H. Selke, R. Chierchia, R. Ebel, S. Einfeldt, and D. Hommel, "X-ray scattering from GaN epitaxial layers - an example of highly anisotropic coherence," *J. Phys. D. Appl. Phys.*, vol. 34, no. 10A, pp. A25–A29, 2001.

[126] R. Chierchia, T. Böttcher, H. Heinke, S. Einfeldt, S. Figge, and D. Hommel, "Microstructure of heteroepitaxial GaN revealed by x-ray diffraction," *J. Appl. Phys.*, vol. 93, no. 11, p. 8918, 2003.

[127] W. D. Nix and B. M. Clemens, "Crystallite coalescence: A mechanism for intrinsic tensile stresses in thin films," *J. Mater. Res.*, vol. 14, no. 08, pp. 3467–3473, Aug. 1999.

[128] B. P. Gunning, E. A. Clinton, J. J. Merola, W. A. Doolittle, and R. C. Bresnahan, "Control of ion content and nitrogen species using a mixed chemistry plasma for GaN grown at extremely high growth rates >9 μm/h by plasma-assisted molecular beam epitaxy," *J. Appl. Phys.*, vol. 118, no. 15, p. 155302, 2015.

[129] B. M. McSkimming, C. Chaix, and J. S. Speck, "High active nitrogen flux growth of GaN by plasma assisted molecular beam epitaxy," *J. Vac. Sci. Technol. A Vacuum, Surfaces, Film.*, vol. 33, no. 5, p. 05E128, Sep. 2015.

[130] E. A. Akhadov, D. E. Read, A. H. Mueller, J. Murray, and M. A. Hoffbauer, "Innovative approach to nanoscale device fabrication and low-temperature nitride film growth," *J. Vac. Sci. Technol. B Microelectron. Nanom. Struct.*, vol. 23, no. 6, p. 3116, 2005.

[131] C. N. Cochran and L. M. Foster, "Vapor Pressure of Gallium, Stability of Gallium Suboxide Vapor, and Equilibria of Some Reactions Producing Gallium Suboxide Vapor," *J. Electrochem. Soc.*, vol. 109, no. 2, p. 144, 1962.

[132] V. Holy, U. Pietsch, and T. Baumbach, "High-resolution X-ray scattering from thin films and multilayers," in *Springer Tracts in Modern Physics*, vol. 149, 1999, p. 251.

[133] E. R. Glaser, T. A. Kennedy, K. Doverspike, L. B. Rowland, D. K. Gaskill, J. A. Freitas Jr., M. Asif Khan, D. T. Olson, J. N. Kuznia, and D. K. Wickenden, "Optically detected magnetic resonance of GaN films grown by organometallic chemical-vapor deposition," *Phys. Rev. B*, vol. 51, no. 19, pp. 326–336, 1995.

[134] A. M. Dabiran, A. V. Osinsky, P. P. Peter, R. C. Fitch, N. Moser, A. Crespo, T. J. Anderson, F. Ren, R. Khanna, L. Stafford, and S. J. Pearton, "GaN-Based Devices for Reliable Operation at Very High Temperatures," in *ECS Transactions*, 2006, vol. 3, no. 9, pp. 349–357.

[135] D. Maier, M. Alomari, N. Grandjean, J.-F. Carlin, M.-A. Diforte-Poisson, C. Dua, A. Chuvilin, D. Troadec, C. Gaquiere, U. Kaiser, S. L. Delage, and E. Kohn, "Testing the Temperature Limits of GaN-Based HEMT Devices," *IEEE Trans. Device Mater. Reliab.*, vol. 10, no. 4, pp. 427–436, Dec. 2010.

[136] J. R. Lang, N. G. Young, R. M. Farrell, Y. R. Wu, and J. S. Speck, "Carrier escape mechanism dependence on barrier thickness and temperature in InGaN quantum well solar cells," *Appl. Phys. Lett.*, vol. 101, pp. 1–5, 2012.

[137] C. J. Neufeld, S. C. Cruz, R. M. Farrell, M. Iza, S. Keller, S. Nakamura, S. P. Denbaars, J. S. Speck, and U. K. Mishra, "Observation of positive thermal power coefficient in InGaN/GaN quantum well solar cells," *Appl. Phys. Lett.*, vol. 99, pp. 2011–2014, 2011.

[138] L. Sang, M. Liao, Y. Koide, and M. Sumiya, "Temperature and Light Intensity Dependence of Photocurrent Transport Mechanisms in InGaN $p - i - n$ Homojunction Solar Cells," *Jpn. J. Appl. Phys.*, vol. 52, p. 08JF04, 2013.

[139] X.-M. Cai, S.-W. Zeng, and B.-P. Zhang, "Favourable photovoltaic effects in InGaN pin homojunction solar cell," *Electron. Lett.*, vol. 45, no. 24, p. 1266, 2009.

[140] X.-M. Cai, S.-W. Zeng, X. Li, J.-Y. Zhang, S. Lin, A.-K. Lin, M. Chen, W.-J. Liu, S.-X. Wu, and B.-P. Zhang, "Dependence of the Property of InGaN p-i-n Solar Cells on the Light Concentration and Temperature," *IEEE Trans.*

Electron Devices, vol. 58, no. 11, pp. 3905–3911, Nov. 2011.

[141] H. M. Branz, W. Regan, K. J. Gerst, J. B. Borak, and E. A. Santori, "Hybrid solar converters for maximum exergy and inexpensive dispatchable electricity," *Energy Environ. Sci.*, vol. 8, no. 11, pp. 3083–3091, 2015.

[142] A. M. Fischer, S. Srinivasan, F. A. Ponce, B. Monemar, F. Bertram, and J. Christen, "Time-resolved cathodoluminescence of Mg-doped GaN," *Appl. Phys. Lett.*, vol. 93, no. 15, p. 151901, 2008.

[143] J.-H. Yun, E. Lee, H.-H. Park, D.-W. Kim, W. a Anderson, J. Kim, N. M. Litchinitser, J. Zeng, J. Yi, M. M. D. Kumar, and J. Sun, "Incident light adjustable solar cell by periodic nanolens architecture," *Sci. Rep.*, vol. 4, p. 6879, Nov. 2014.

[144] A. Maros, S. Gangam, Yi Fang, J. Smith, D. Vasileska, S. Goodnick, M. I. Bertoni, and C. B. Honsberg, "High temperature characterization of GaAs single junction solar cells," in *2015 IEEE 42nd Photovoltaic Specialist Conference (PVSC)*, 2015, pp. 1–5.

[145] A. Asgari and K. Khalili, "Temperature dependence of InGaN/GaN multiple quantum well based high efficiency solar cell," *Sol. Energy Mater. Sol. Cells*, vol. 95, no. 11, pp. 3124–3129, Nov. 2011.

[146] K. Y. Lai, G. J. Lin, Y.-R. Wu, M.-L. Tsai, and J.-H. He, "Efficiency dip observed with InGaN-based multiple quantum well solar cells.," *Opt. Express*, vol. 22 Suppl 7, no. December, pp. A1753–60, 2014.

[147] R. H. Horng, S. T. Lin, Y. L. Tsai, M. T. Chu, W. Y. Liao, M. H. Wu, R. M. Lin, and Y. C. Lu, "Improved conversion efficiency of GaN/InGaN thin-film solar cells," *IEEE Electron Device Lett.*, vol. 30, no. 7, pp. 724–726, 2009.

[148] Y. Zhang, M. J. Y. Tayebjee, S. Smyth, M. Dvořák, X. Wen, H. Xia, M. Heilmann, Y. Liao, Z. Zhang, T. Williamson, J. Williams, S. Bremner, S. Shrestha, S. Huang, T. W. Schmidt, and G. J. Conibeer, "Extended hot carrier lifetimes observed in bulk In0.265±0.02Ga0.735N under high-density photoexcitation," *Appl. Phys. Lett.*, vol. 108, no. 13, p. 131904, Mar. 2016.